UNIVERSIDAD DE CHILE
FACULTAD DE CIENCIAS FÍSICAS Y MATEMÁTICAS
DEPARTAMENTO DE INGENIERÍA ELÉCTRICA

DEVELOPMENT AND ANALYSIS OF A LOCALIZATION METHODOLOGY FOR FEMTO-SATELLITES USING TWO CUBESATS IN SPACE

TESIS PARA OPTAR AL GRADO DE DOCTOR EN INGENIERÍA ELÉCTRICA

MATÍAS GABRIEL VIDAL VALLADARES

PROFESOR GUÍA::
MARCOS ANDRÉS DÍAZ QUEZADA

MIEMBROS DE LA COMISIÓN:
SHINICHI NAKASUKA
MARCOS ORCHARD CONCHA
ESTEBAN VERA ROJAS

SANTIAGO DE CHILE
2023

RESUMEN DE LA TESIS PARA OPTAR AL GRADO DE
DOCTOR EN INGENIERÍA ELÉCTRICA
AUTOR: MATÍAS GABRIEL VIDAL VALLADARES
FECHA: 2023
PROFESOR GUÍA: DR. MARCOS ANDRÉS DÍAZ QUEZADA

DESARROLLO Y ANÁLISIS DE UNA METODOLOGÍA DE LOCALIZACIÓN PARA FEMTO-SATÉLITES USANDO DOS CUBESATS EN EL ESPACIO

La reducción del tamaño, tiempo de desarrollo, y costo, ha facilitado la proliferación de constelaciones de pequeños satélites. Un interés particular por estas constelaciones está relacionado con medir el ambiente espacial. Los satélites requeridos para modelarlo usualmente son del orden de los cientos. Hay una falta de mediciones en alturas bajo los 380 km. Estas alturas requieren una gran cantidad de propelente para mantener un satélite en órbita, haciendo que esta región sea infactible. Los femto-satélites, cuya masa es menor a 100 g, pueden resolver este problema. En el laboratorio SPEL desarrollamos dos CubeSats, SUCHAI-2 y SUCHAI-3. Este último transporta un femto-satélite, y necesitamos estimar su posición para cada medición. Se propone un método para estimar la posición del femto-satélite usando el TDOA y el AOA de sus balizas a los dos CubeSats. También se demuestra que el desempeño del método de localización está directamemte relacionado con la dirección de despliegue del femto-satélite y la geometría formada por los tres satélites. El 84,6% de los escenarios simulados tienen un RMSE menor a 30 m. Mediante un modelo dinámico de la órbita, se reduce el error de los demás casos de alrededor de 10^8 km a un máximo de 3,41 km.

ABSTRACT OF THE THESIS FOR THE DEGREE OF
DOCTOR IN ELECTRICAL ENGINEERING
AUTHOR: MATÍAS GABRIEL VIDAL VALLADARES
DATE: 2023
ADVISOR: DR. MARCOS ANDRÉS DÍAZ QUEZADA

DEVELOPMENT AND ANALYSIS OF A LOCALIZATION METHODOLOGY FOR FEMTO-SATELLITES USING TWO CUBESATS IN SPACE

The reduction in size, development time, and cost have facilitated the proliferation of satellite constellations composed of miniaturized satellites. A particular interest in these constellations is related to probing the space environment. The desired number of satellites required for this usually falls in the hundreds. There is a lack of measurements at altitudes below 380 km. These altitudes require significant propulsion to maintain large satellites, making them unfeasible for that region. Femto-satellites, which have a mass of less than 100 g, can solve this problem. At the Space and Planetary Exploration Laboratory (SPEL), we developed two CubeSats, SUCHAI-2 and SUCHAI-3. The latter carries a femto-satellite, and we need to estimate its position for each measurement. I propose a method to estimate the femto-satellite position using its beacons' TDOA and AOA at two CubeSats. I also demonstrate that the performance of the localization method is directly related to the femto-satellite's direction of deployment and the geometry formed by the three satellites. The 84.6% of the simulated scenarios have an RMSE of less than 30 m. Using an orbit's dynamic model, the error of the rest of the cases is reduced from around 10^8 km to a maximum of 3.41 km.

A mi Señor Jesucristo, quien nos amó desde antes
de la fundación del mundo, dio su vida por nosotros,
resucitó al tercer día, y ahora reina.
A mi papá, que descansa en la presencia del Señor.
A mi mamá por amarme y cuidarme siempre,
y a mi amada novia Sarani por su amor
y apoyo incondicional.

Acknowledgments

First, I would like to thank my Lord Jesus Christ, for giving me the strength to finish this work. To my brothers and sisters in Christ, and to my family and friends, thank you for your prayers, love, and support.

I also want to thank ANID for funding my Thesis under the grant CONICYT-PFCHA/2017-21171111.

I am grateful for all the help and support of the whole SPEL team, especially Professor Marcos Díaz for his advice and understanding during the difficult times.

I am thankful for the SEELA students exchange program which allowed me to do an internship at the University of Tokyo. I remember the kindness and hospitality of Professor Shinichi Nakasuka during my stay, and also the diligence of the team at the Intelligent Space Systems Laboratory (ISSL) when I had a question or when I needed something.

I want to thank Professor Aroh Barjatya, who received us at his laboratory at the Embry-Riddle Aeronautical University. During our stay, we finished the final details and calibrated the magnetometers of SUCHAI-2, SUCHAI-3, PlantSat, and FE1.

Finally, I am very thankful for the UNNATI program, organized by U R RAO Satellite Centre and the Indian Space Research Organisation (ISRO). I learned a lot about satellites, their subsystems, integration, and testing. I met wonderful people and made good friends from all over the world.

Table of content

List of Tables

List of Figures

1. Introduction

1.1 Motivation

Wireless localization schemes have been used for years to determine the position of a target. One of the applications is the wireless sensor networks (WSNs) which consist of sensors monitoring a region to measure some local quantity of interest. These networks are used for event detection, exploration, and surveillance, among other applications [3]. To decrease the cost, only a few sensors are equipped with a GNSS receiver. The rest of the sensors use this data to determine their position. This is done with range-based methods such as Received Signal Strength (RSS) [3, 4, 5, 6, 7], Time Of Arrival (TOA) [6, 7, 8], Time Difference Of Arrival (TDOA) [6, 7, 9, 10, 11, 12], Frequency Of Arrival (FOA) [7], Frequency Difference Of Arrival (FDOA) [7], and Angle Of Arrival (AOA) [3, 4, 5, 6, 7, 8, 10].

Wireless sensor networks on the ground have many limitations and sources of noise, such as Non-Line-Of-sight (NLOS) scenarios, multipath, adverse weather conditions, and co-channel interference, among many others. However, in space applications, there are many advantages. Earth itself is the main obstacle to the Line-Of-Sight (LOS). There is no multipath, and the International Telecommunication Union (ITU) regulates the satellite's frequencies to avoid interference as much as possible. The satellites are not affected by the same weather conditions as the ground networks, like rain and thunderstorms. There are other noise sources, such as solar flares, Coronal Mass Ejections (CMEs), and the South Atlantic Anomaly (SAA), to name a few, that are detrimental to the satellite's communication and measurements.

Location estimation for satellites is relevant for many reasons, such as establishing communication with the ground station(s), operating the payload (e.g., imaging over a particular region), and orbital maneuvering, among many others. The location estimation of satellites can be either passive or active. A passive solution requires no action from the satellite to estimate its location. An example of localization systems with passive methods are ground- and space-based (located in other satellites) radars or telescopes. North American Aerospace Defense Command (NORAD) continuously monitors all objects orbiting the Earth with radar installations in the USA and Canada. Leolabs is a company that focuses on the Low Earth Orbit (LEO) and uses phased-array radars to locate the satellites. Neither NORAD nor Leolabs requires the satellite to have special hardware to obtain its position. However, the satellite is unaware of its position unless it receives it. An active

solution requires some action from the satellite to estimate its location. The Global Navigation Satellite System (GNSS) and Doppler Orbitography and Radiopositioning Integrated by Satellite (DORIS) [13] are examples of active solutions. The GNSS relies on a satellite network that sends continuous synchronized radio signals to a receiver in the spacecraft, which estimates its location from the multiple received signals. In contrast, DORIS relies on multiple measurements of the Doppler shift of signals sent from ground stations to obtain an accurate estimation.

The reduction in size, time of development, and cost have facilitated the proliferation of a new spectrum of space missions based on satellite constellations or swarms composed of hundreds and even thousands of spacecraft. These spacecraft can be nano-satellites, such as CubeSats, or even femto-satellites carried by CubeSats [14, 15]. The potential applications of these constellations are varied, especially for science. Having multiple sensors in space allows researchers to differentiate temporal changes from spatial ones in the measurements. A particular type of mission where this number of spacecraft can be relevant is related to probing the space environment to help understand the impact solar activity has on the ionosphere and the high atmosphere (e.g., [16, 17, 18]) by using miniaturized sensors in them (e.g., [16, 19]). The desired number of satellites required to model the space dynamics usually falls in the hundreds. Moreover, there is a lack of measurements at altitudes below 380 km, where significant propulsion is required to maintain large satellites at those altitudes, making them unfeasible for that region. A potential alternative is to use femto-satellites, which have a mass of less than 100 g. The small size of this type of satellite allows an extremely low-cost development. Even if they fall to earth fast, they are so inexpensive that it is more convenient to replace them than using propulsion to keep them in orbit. Nevertheless, the complication of using these miniaturized satellites for space weather applications is the requirement of the location estimation of the satellites. In femto-satellites, it is possible to use Commercial-Off-The-Shelf (COTS) components for every subsystem, except for the location system, which is necessary for many space applications. Although a GNSS receiver is appropriate for a CubeSat, it is not for a femto-satellite. A GNSS receiver with the license to operate in space costs around USD 2000. This cost can be prohibitive for a constellation of thousands of femto-satellites that might have an ephemeral operational life in space. Cost aside, the power budget of a femto-satellite is not enough to handle the continuous operation of a GNSS receiver [20].

In the Space and Planetary Exploration Laboratory (SPEL) at the University of Chile, we are working on developing such types of missions, with a preliminary technology demonstration that is inside one of the missions of the laboratory [21]. Preliminary, we plan to deploy a femto-satellite version that contains a GPS to verify the position. This version will carry a magnetometer and a miniaturized particle counter that was tested in the SUCHAI-1 mission [22]. We will deploy the femto-satellite opportunistically to increase the sensing points in the ionosphere/magnetosphere. This increase in the sensing points allows us to study the dynamic evolution during a geomagnetic storm. An ionospheric/magnetospheric anomalous activity usually lasts for a couple of days [23]. This duration requires the femto-satellite to operate for a few days. The experiment will be with two 3U CubeSats, the SUCHAI-2 and SUCHAI-3 (Figure 1.1). Both CubeSats were launched on April first, 2022 inside a Falcon 9 rocket. They were carried inside a D-orbit

satellite carrier which put them in orbit. SUCHAI-3 will serve as the mother spacecraft of the femto-satellite, carrying and deploying it at some moment once in orbit. The femto-satellite will send the gathered data with a radio communication link to both CubeSats. In this research, we simulate a similar scenario to study the feasibility of using the radio links to estimate the location of a femto-satellite with only two CubeSats. This location estimation combines the Time Difference Of Arrival (TDOA) with the Angle Of Arrival (AOA) of the received signals.

Figure 1.1: Images of the SUCHAI-2 and -3 CubeSats during the integration process together with part of the development team at the Space and Planetary Exploration Laboratory (SPEL). These CubeSats were launched on April first, 2022. They carry magnetometers and an S-band communication system to receive the data from a femto-satellite. The femto-satellite also has a magnetometer, and it will be carried and deployed by the SUCHAI-3 CubeSat. I am studying the feasibility of estimating the location of a radio source (femto-satellite) in a concrete scenario, in low earth orbit where there are only two CubeSats available to estimate the location of a femto-satellite.

The TDOA method has been used for drone detection and localization [24], in storehouse environments [25], IoT [26] and by mobile users [27]. This method has also been used on larger satellites, using it to localize a satellite from the ground [28], as well as from other satellites in space [29]. The AOA method uses an antenna array to know the yaw (azimuth) and pitch (elevation) of the received signal. Placing the antennas in a square array [30] allows for estimating both yaw and pitch instead of just one angle. A target can send a signal to multiple receivers with antenna arrays. The angles measured at the receivers with known locations provide the target position. This method has been used mostly on the ground for wireless sensor networks [3]. There is also research for the 5G cellular system, which uses antenna arrays in the stations, suggesting the possibility of locating a phone

using the AOA with multiple transmission-reception points [31]. A work even suggested using two satellites to passively locate an object on the surface of the Earth using TDOA, Frequency Difference Of Arrival (FDOA), and AOA measurements [32]. Figure 1.2 shows our implementation of an antenna array.

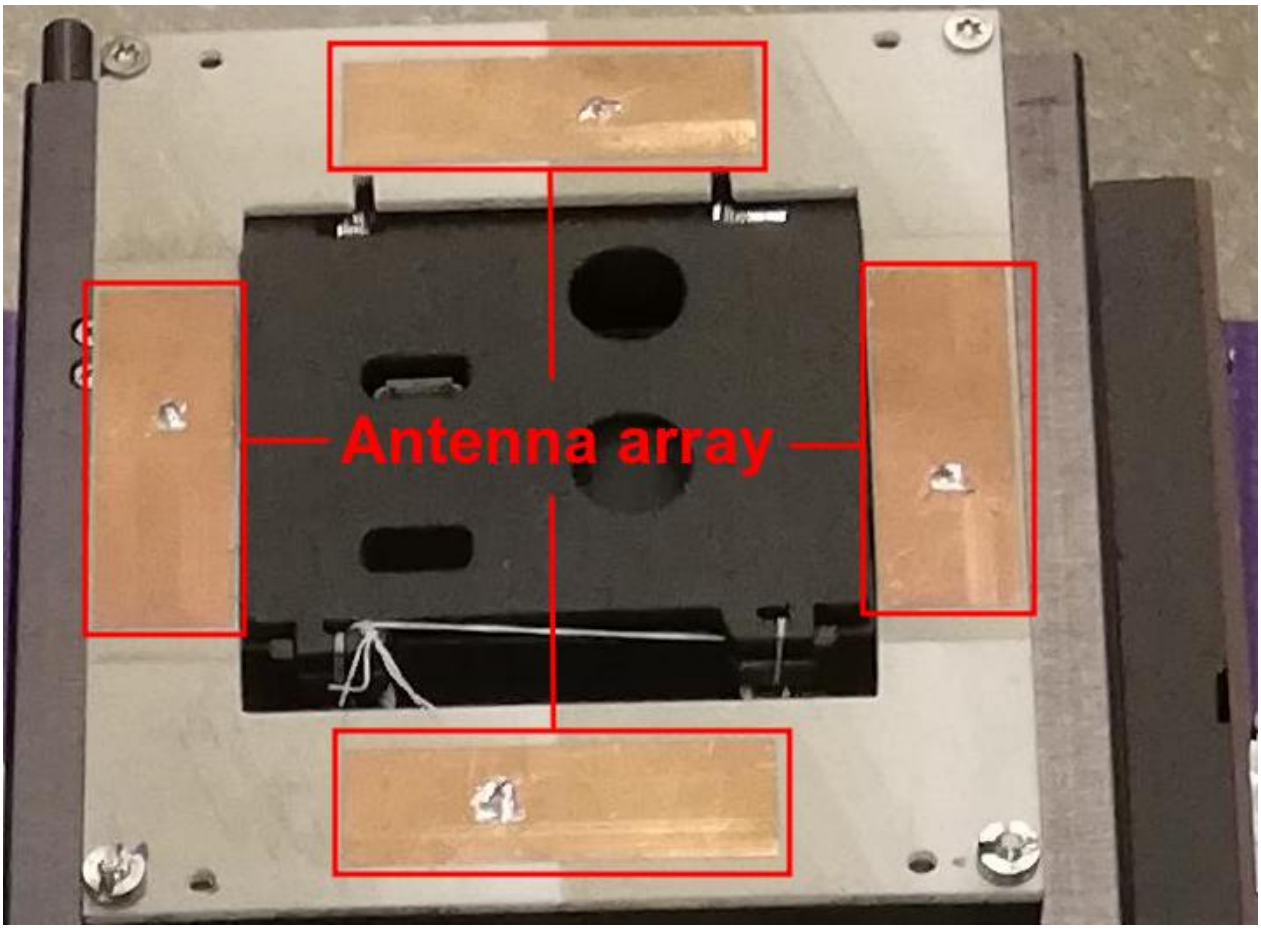

Figure 1.2: We developed an antenna array able to fit in one face of the CubeSat. This figure shows a four-antenna array located at the side of the satellite, with the gate of the femto-satellite deployment system in the middle. We will deploy the femto-satellite through this gate made of Windform.

I based my work on Yin et al. [33] localization method. Yin et al. estimated the location of a source using two stations in fixed and well-known positions. My work studies the accuracy of this method when the stations are moving and have uncertainty in their positions. I study the performance of this method in the context of space. In this context, the stations are now CubeSats separated by 30 km and moving in a polar orbit. The position of these CubeSats is changing but is also affected by the accuracy of the onboard GNSS receivers. The source is a femto-satellite deployed from one of the CubeSats at a certain speed and direction (which I will determine in the next sections). I evaluate if different positions and directions of deployment change the performance of the localization method. The simulation of the deployment direction considers that the

Attitude Determination and Control System (ADCS) is not perfect. The CubeSats combine range-based (TDOA) and angle-based (AOA) localization methods to estimate the femto-satellite position through the communication link. Each CubeSat is assumed to carry an antenna array, an ADCS, and a GNSS receiver. In my study, the femto-satellite transmits a beacon to the CubeSats, and the CubeSats then measure the beacon TDOA and AOA using antenna arrays. These CubeSats relay this information to the ground station, which combines it to estimate the femto-satellite position. I study the effect on the Cramér–Rao Bound (CRB) and the Root-Mean-Square Error (RMSE) of the femto-satellite location for different deployment directions, CubeSats location, and attitude determination and control precision. To evaluate the location precision, I developed a simulation tool that emulates the orbit of the satellites using the SGP4 model [34]. This simulation tool was developed in Python and made available to the community as an open-source tool. It is hosted in the SPEL's GitHub site at the following link (last accessed on February 23rd, 2023): `https://github.com/spel-uchile/Pypredict`.

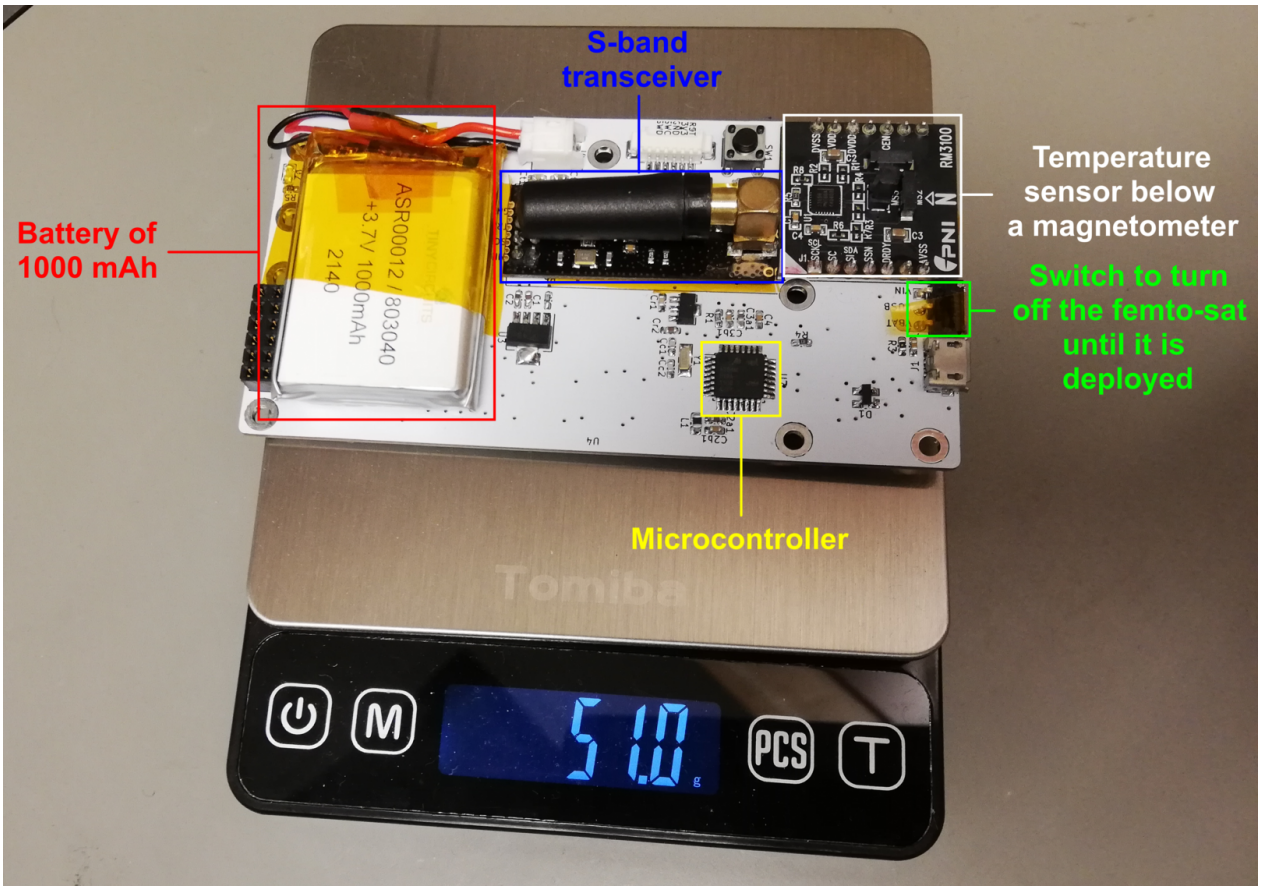

Figure 1.3: This is a picture of the femto-satellite FE1. The FE1 is currently inside the SUCHAI-3. It has a mass of 51 g and carries a PNI RM3100 magnetometer, an MCP9808 temperature sensor, a 1000 mAh battery, an nRF24L01+ S-band transceiver, and a SAMD21E microcontroller. We use the temperature sensor to calibrate the magnetometer's measurements. The gate of the Femto-satellite Orbital Deployer (FOD) is closing the switch, which prevents the femto-satellite from turning on before time. When the FOD's gate is opened, the femto-satellite will turn on and take some measurements to later send them to the SUCHAI-3. The SUCHAI-2 can also receive data from FE1.

1.2 Hypothesis

H1 The position of a femto-satellite can be estimated using only two CubeSats with GNSS receivers, antenna arrays, and a communication link with the femto-satellite.

H2 The position estimation error varies at least one order of magnitude depending on the direction of deployment of the femto-satellite, the position of deployment, and the accuracy of the mother-CubeSat's ADCS.

H3 There are situations when the position estimation error can be reduced by at least two orders of magnitude using a dynamic model of the orbit instead of the measurements.

1.3 Objectives

1.3.1 General objectives

To simulate the position estimation of a femto-satellite using two CubeSats in Low Earth Orbit (LEO). The results of this research, together with the derived software will be open for the small-satellite community to use and improve.

1.3.2 Specific objectives

The following objectives are the necessary steps to accomplish the general goal.

- To simulate a localization system in which a femto-satellite sends a signal to two CubeSats. The CubeSats will estimate the femto-satellite's position using the Time Difference Of Arrival (TDOA) and Angle Of Arrival (AOA) methods. This localization system must consider the accuracy of the GNSS receivers and the antenna arrays.
- To evaluate the performance of this system in terms of accuracy for different deployment directions and positions and ADCS accuracies. This evaluation must include the simulation of a complete orbit starting three days after the deployment of the femto-satellite.
- To improve the performance of the localization system using a dynamic model of the femto-satellite's orbit when the uncertainty of the measurements increases.

1.4 Contributions

The main contributions of my Thesis to the state-of-the-art and the small-satellite community are the following:

- The development of an open-source orbit propagator that uses the TLE set and the SGP4 method to display the position of multiple satellites for a given time. It also

displays the day/night terminator, the satellite coverage, and the ground track, and it can be used to simulate the deployment of a satellite from another one.

- I demonstrate with simulations that it is possible to estimate the position of a femto-satellite using only two CubeSats and the communication link between them.
- To simulate the deployment of a femto-satellite from a CubeSat and to show which deployment direction allows us to perform better for the AOA and TDOA localization methods.
- It improves the position estimation with an orbit model when the uncertainty of the measurements increases the position error over two kilometers.
- I published this work in the journal Remote Sensing (`https://doi.org/10.3390/rs14051101`) titled: *"A Femto-Satellite Localization Method Based on TDOA and AOA Using Two CubeSats"* [35].

2. State of the art

2.1 Satellite navigation

The first artificial Earth satellite, Sputnik 1, was launched on 4 October 1957 by the Soviet Union. Three days later, Dr. William H. Guier and Dr. George C. Weiffenbach calculated its orbit using the Doppler shift as a proof of concept. They published this method applied to the first satellite launched by the US, called Explorer 1, in 1958 [36]. After this, Dr. Frank T. McClure asked them if they could solve the inverse problem: to locate an object using satellites. A year later, they laid the foundations for a project called Transit [37]. This project was used to provide navigation for the US Navy using satellite radio navigation. Transit demonstrated that a space system could enable a ground receiver to estimate its position in 2D using the satellite's Doppler shift. This system entered the Naval service in 1964, and it was made available to the general public in 1967 until 1996 when it was retired. Another project, called Timation, was developed by the US Naval Research Laboratory (NRL) to test the feasibility of placing highly accurate clocks into orbit, aiming for worldwide coverage [38]. The first Timation satellite was launched on 31 May 1967. In 1963, the Air Force Space Systems Division started a classified project called 621B for a space-based navigation system. In 1973, the Timation program was merged with the 621B project, and the last two Timation satellites were redesignated as NTS-1 and NTS-2, the prototypes for the Global Positioning System (GPS) [39, 40].

A system that uses satellites for geospatial positioning is called a satellite navigation system or satnav. These systems provide Positioning, Navigation, and Timing (PNT) service. Some systems cover a particular region, like Japan's Quasi-Zenith Satellite System (QZSS) [41] and the Indian Regional Navigation Satellite System (IRNSS) [42], and others that are available around the Earth called Global Navigation Satellite Systems (GNSS). There are four GNSS: The GPS, GLONASS, Beidou, and Galileo.

2.1.1 Global Positioning System (GPS)

The GPS is a constellation of at least 24 satellites (31 currently [43]) in six different orbital planes, equipped with very stable atomic clocks. They fly in Medium Earth Orbit (MEO) at an altitude of approximately 20,200 km. The latest Space Vehicle (SV), GPS III SV06, was launched on January 18th, 2023 aboard a SpaceX Falcon 9 rocket. All satellites broadcast at the same frequencies, encoding signals using unique Code-Division Multiple Access (CDMA) so receivers can distinguish individual satellites from each other. Each

SV continuously broadcasts in different RF links called L1 (1575,42 MHz), L2 (1227,60 MHz), and L5 (1176,45 MHz). In each RF link, the SV transmits the modulo-2 addition of a Pseudo-Random Noise (PRN) ranging code with the navigation data D(t).

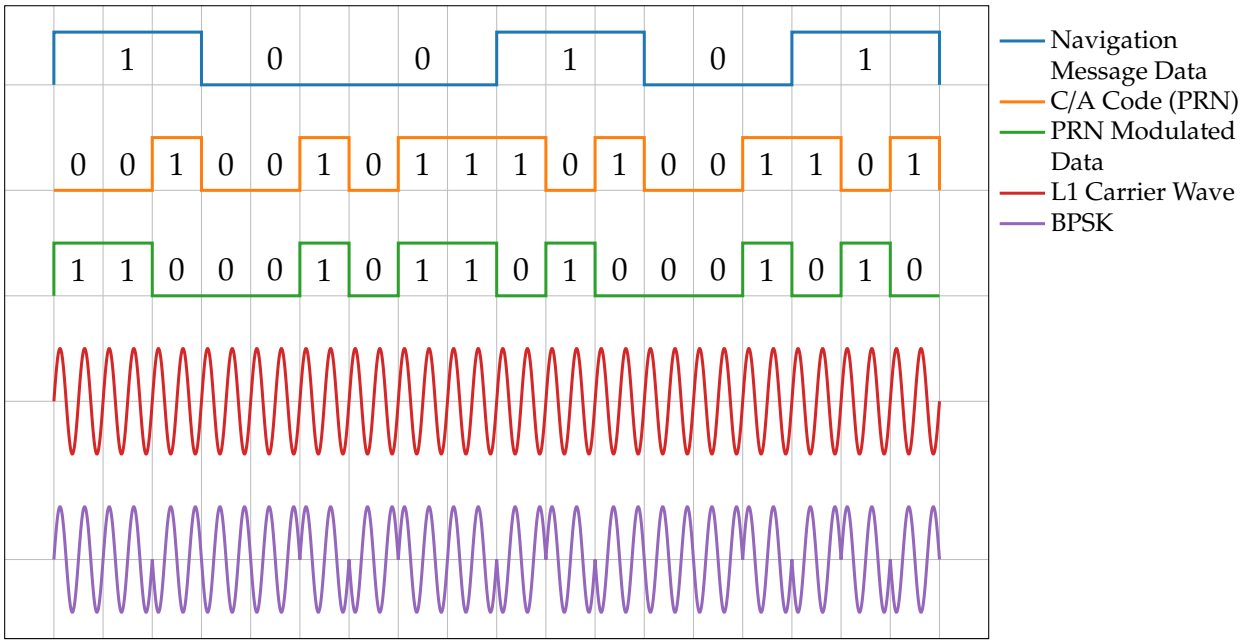

Figure 2.1: This example shows the BPSK modulation of the modulo-2 addition of the navigation data with the C/A code. The blue line shows the navigation data. This data contains the SV ephemerides, system time, SV clock behavior, and other information. The orange line is the C/A code used only by that SV at that moment. The green line is the modulo-2 addition of the navigation data and the C/A code. The red line is the carrier wave, and the purple line is the BPSK signal containing the information of the green line.

The PRN ranging code is a sequence of zeros and ones different for each satellite, and the receiver knows it. Originally, there were only three PRN ranging codes being transmitted: The Precision (P) code, which is the principal navigation ranging code at a chipping rate of 10.23 Mbps; The Y code, which is used instead of the P-code for the anti-spoofing mode; and the Coarse/Acquisition (C/A) code at a chipping rate of 1023 kbps. The C/A code is the civil ranging signal, and it is also used to acquire the P or Y code (denoted as P(Y)). There are multiple generations of SVs, and they are divided by blocks. The Blocks IIR-M, IIF, and future blocks transmit two additional PRN ranging codes. They are the L2 Civil-Moderate (L2 CM) code and the L2 Civil-Long (L2 CL) code, both at 511.5 kbps [44]. The legacy navigation data includes the SV ephemerides, system time, SV clock behavior data, status messages, and C/A to P (or Y) code handover information at 50 bps.

Multiple factors can degrade the performance of a GPS receiver. Some of them are satellite clock errors, ionospheric effects, multipath, and ephemeris errors. Dual-frequency GPS receivers can reduce the effects of the ionosphere in position estimation. An accuracy assessment of dual frequency receivers for aircraft obtained an accuracy of less than 3.4 m in the geocentric XYZ coordinates in 2020 [45].

SV Blocks	**L1**		**L2**	
	In-Phase	Quadrature-Phase	In-Phase	Quadrature-Phase
Block IIR	P(Y) $\oplus$ D(t)	C/A $\oplus$ D(t)	P(Y) $\oplus$ D(t) or P(Y) or C/A $\oplus$ D(t)	Not Applicable
Block IIR-M/IIF and GPS III/IIIF	P(Y) $\oplus$ D(t)	C/A $\oplus$ D(t)	P(Y) $\oplus$ D(t) or P(Y)	L2 CM $\oplus$ D_c(t) with L2 CL or C/A $\oplus$ D(t) or C/A

Table 2.1: This table shows some of the codes used in L1 and L2 links. The D(t) is the navigation data at 50 bps, and D_c(t) is the navigation data at 25 bps with Forward Error Correction (FEC) encoding resulting in 50 sps.

2.1.2 GLONASS

The GLONASS constellation has 24 satellites in operation and one in the commissioning phase. These satellites are in three orbital planes inclined at 64.8° to the equator. They have a roughly circular orbit with an altitude of 19,100 km. Like the GPS constellation, it uses the Direct-Sequence Spread Spectrum (DSSS) and BPSK modulation. Traditionally, GLONASS uses the Frequency Division Multiple Access (FDMA) techniques, but as part of its modernization, it also uses the CDMA technique [46].

2.1.3 BeiDou

The BeiDou constellation has 44 operational satellites. Seven are in Geostationary Orbit (GEO), 10 in 55° inclined geosynchronous orbits, and 27 in MEO divided into three planes. It uses the CDMA principle like other GNSS constellations. BeiDou also has public and military positioning services. All BeiDou satellites have laser retro-reflector arrays for high-precision range measurements. [47, 48].

2.1.4 Galileo

The Galileo constellation has 24 satellites in three orbital planes inclined at an angle of 56° to the equator. Three independent CDMA signals, named E5, E6, and E1, are permanently

transmitted by all Galileo satellites. The E5 signal is subdivided into two signals denoted E5a and E5b [49].

2.1.5 Challenges for space-borne GNSS receivers

There are multiple low-cost GNSS receivers for ground applications, such as smartphones, tablets, and vehicle GNSS units. The GNSS receivers for space missions need to perform at speeds of at least 7,5 km/s, which increases the Doppler shift and demands an increased dynamic range in signal power due to the variations in the distance to the GNSS satellites. Like any device sold for satellite applications, the space-borne GNSS receivers require thorough tests to ensure they will function during the entire spacecraft mission. Some of the tests are the radiation test, the thermo-vacuum test, and the vibration test. There are some restrictions on the export of these devices due to the risk of being used for intercontinental ballistic missile-like applications. For this restriction, it is necessary to pay a license to operate in space. All these reasons increase the cost and power consumption of these receivers.

Item	TRH-G2	NSS GPS	NanoSense GPS	GPSRM 1
Accuracy [m]	-	< 10.0	1.5	1.5
Power consumption [W]	> 1.0	> 1.0	> 1.3	> 0.9
Price [US$]	> 1800	-	-	> 10,485
Mass [g]	> 14	< 130	> 31	109
Dimensions [mm]	84 x 29 x 11	96 x 91 x 18	46 x 72 x 11	96 x 90 x 18

Table 2.2: This table has some space-grade GNSS receivers for nano-satellites or smaller ones. The NSS GPS and the GPSRM 1 have the PC/104 form factor. The NanoSense GPS needs to be mounted on another PCB. That PCB also uses the PC/104 standard. Only the TRH-G2 could fit in a femto-satellite, but its cost and power consumption are too high for continuous operation.

Most of the smaller GNSS receivers for space applications are intended for CubeSats. One of the most widely used PCB standards for CubeSats is the PC/104. This standard has a form factor of around 90 mm x 96 mm. The boards that follow this standard connect with each other electrically using a male-to-female connector, one on top of the other. These boards also have four mounting holes, one in each corner of the PCB. The PCBs are secured in place with stack rods and separators between boards. This design works well for CubeSats, but the size is too big for a femto-satellite. Commercially available CubeSat structures can not deploy a femto-satellite with the PC/104 form factor due to the mechanical conflict between the board, the satellite structure, and the stack rods. For these reasons, a GNSS device for CubeSats is not compatible with a femto-satellite.

2.2 Orbit propagation

2.2.1 Orbital elements

The orbit of a satellite can be described using Cartesian coordinates. For example, using the Earth-Centered Inertial (ECI) coordinate frame to describe six elements: position and velocity in three axes. Another way to describe an orbit is by using six Keplerian elements. These elements, also known as orbital elements, describe a non-inertial trajectory of a body around another body with more mass.

- Eccentricity (e): Describes how elongated is the shape of the orbit compared to a circle.
- Semimajor axis (a): This distance can be obtained by adding the periapsis with the apoapsis and dividing them by two.
- Inclination (i): The angular momentum vector $\boldsymbol{h}$ is normal to the plane of the orbit. The inclination is the angle between this vector and the positive $\boldsymbol{Z}$ axis.
- Right Ascension of the Ascending Node (Ω): The node line vector $\boldsymbol{N}$ extends outward from the origin through the ascending node. The angle between the $\boldsymbol{X}$ axis and $\boldsymbol{N}$ is Ω.
- Argument of the perigee (ω): It is the angle formed by the Node line vector and the eccentricity vector.
- True anomaly (ν, θ or f): It is an angle between the direction of the periapsis and the position of the satellite in the orbit.

2.2.2 Simplified General Perturbations-4 model (SGP4)

The Simplified General Perturbations-4 model (SGP4) is used to propagate and calculate the orbital elements of satellites and space debris. It considers the effect of orbital perturbations like the atmospheric drag, the effects of the Earth's oblateness, and the gravitational perturbations of the sun and the moon [34]. The SGP4 was merged with the SDP4 model to include deep space perturbations. The input for this model is a Two Line Element set (TLE) frequently published by NORAD.

2.2.3 Two Line Element set (TLE)

The Two-Line Element sets (TLE) are the more widely used source of data to obtain the position of the orbiting satellites. It consists of two 69-character lines of data provided by NORAD, that describe the orbit of a satellite. It includes orbital elements such as the inclination, the Right Ascension of the Ascending Node (RAAN), the eccentricity, the argument of the perigee, the mean anomaly, and the mean motion, which are necessary to determine a satellite's position and velocity at a given time. This data is propagated using the SGP4 model. The error of this model increases several kilometers a day [50, 51]. There have been some proposals to improve the orbit prediction accuracy of the SGP4 model [50, 52], but require a model of the propagation error or previous historical data which is not always available. There is also research on improving the position estimation of the

SGP4 model using GPS data [53, 54]. Since the power generation of the femto-satellites is limited, it is relevant to seek another way to measure its position.

Table 2.3: This is the TLE of the International Space Station (ISS), obtained on February 17th, 2023, from `https://celestrak.org/`.

```
1 25544U 98067A   23048.35037287  .00023514  00000+0  41609-3 0  9999
2 25544  51.6397 202.0987 0009448 359.4932 192.9698 15.50140668383207
```

2.3 Range-based and angle-based localization methods

Range-based and angle-based localization systems can replace the need for a GNSS device. These systems, such as TDOA and AOA, can be used simultaneously to improve position estimation. Inter-satellite communication and ranging have been studied for CubeSats. Range-based methods have been proposed, such as RSS, TOA and two-way ranging (TWR) [55]. A Software Defined Radio (SDR) has been used with RSS and TWR for a collision detection system [56].

Many range-based and angle-based localization techniques have been developed. For example, the Received Signal Strength (RSS) method measures the power of a signal sent from an unknown location. The range between the known location and the transmitter is calculated using the Friis equation. This equation forms a circle around the known location. The radius of this circle is the range, and the perimeter is the target's possible location. An intersection of the formed circles can be found with multiple known locations, narrowing the target's location. The RSS system is easy to implement but requires an omnidirectional radiation pattern. If this is not the case, it can increase the errors in the estimations. It also does not perform well on long-range scenarios [1]. A better alternative is to use the Time Difference Of Arrival combined with the Angle Of Arrival (AOA) method.

2.3.1 Time Difference Of Arrival (TDOA)

The TDOA method works by calculating the difference in time between signals sent from known locations. The differences in time are transformed into differences in distance (equation 2.4). These differences in distance outline hyperbolas in 2D and hyperboloids in 3D. The hyperbolas or hyperboloids are the possible locations of the target. The intersection between the hyperboloids indicates the target's location [57]. This intersection can be calculated in terms of the distance between the target and one of the references. Chan did an example in 2D [9], but a 3D expression can also be obtained (see equation 2.1). I can calculate the distance r_1 using the squared definition of the distance between the reference and the target in equation 2.3. This equation is quadratic and returns two solutions for r_1, in which usually one of them can be discarded for being negative. With this result, I can obtain the position of the target.

$$\begin{bmatrix} x \\ y \\ z \end{bmatrix} = -\begin{bmatrix} x_{2,1} & y_{2,1} & z_{2,1} \\ x_{3,1} & y_{3,1} & z_{3,1} \\ x_{4,1} & y_{4,1} & z_{4,1} \end{bmatrix}^{-1} \left(\begin{bmatrix} \tau_{2,1} \\ \tau_{3,1} \\ \tau_{4,1} \end{bmatrix} r_1 + \frac{1}{2} \begin{bmatrix} \tau_{2,1}^2 - C_2 + C_1 \\ \tau_{3,1}^2 - C_3 + C_1 \\ \tau_{4,1}^2 - C_4 + C_1 \end{bmatrix} \right) \tag{2.1}$$

$$C_i = x_i^2 + y_i^2 + z_i^2 \tag{2.2}$$

$$r_i^2 = (x_i - x)^2 + (y_i - y)^2 + (z_i - z)^2 \tag{2.3}$$

$$\tau_{i,1} = r_i - r_1 = c \cdot (t_i - t_1) \tag{2.4}$$

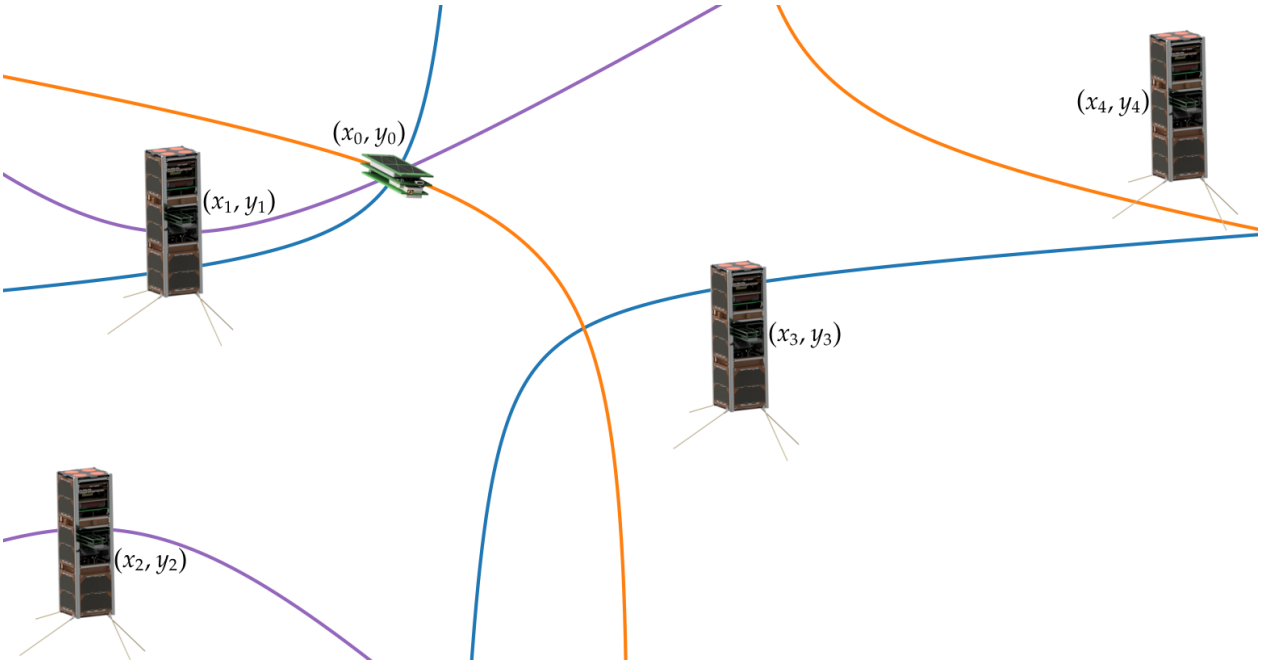

Figure 2.2: The TDOA method consists of obtaining time differences between the arrival of signals sent from different known positions. These time differences translate into distance differences that form hyperbolas or hyperboloids. The intersection of these hyperbolas or hyperboloids is where the target is located. In space, this method can be used with satellites equipped with GNSS receivers used as references and femto-satellites as targets.

There are three main sources of error in TDOA studied in the literature: Clock synchronization, non-line-of-sight (NLOS), and measurement errors of the references [26]. This method does not require synchronization between the target and the CubeSats, but the CubeSats need to be synchronized with each other. It has been reported that using GPS receivers, there is a minimum achievable synchronization offset of 200 ns [58]. In orbit, the only obstacle is our planet, so we can assume we have LOS for our purposes and that there is no multipath. Current space-grade GNSS receivers for CubeSats offer accuracy of less than 10 m (table 2.2). Liu *et al.* used a more conservative 20 m Gaussian noise for their simulation example using GPS receivers, the SGP4 model, and an epoch state Kalman filter [53].

Figure 2.2 shows an example with four CubeSats as references and a femto-satellite as a target. With four CubeSats, it is possible to obtain the target's position [9]. There are some occasions where there may be two solutions. The solution for these cases is to add a restriction using the previous location of the target.

The TDOA method has been used for drone detection and localization [24], in storehouse environments [25], IoT [26] and mobile users [27]. There are also many applications for satellites. Some of them use TDOA to localize a satellite from the ground [28] or from other satellites [29].

2.3.2 Angle Of Arrival (AOA)

The AOA method requires an antenna array to know the azimuth and the elevation of a received signal. Figure 2.3 shows a linear antenna array, with M antennas spaced with a distance d. Assuming that the array is in the far field, the received signal will be planar. If the signal arrives at an angle θ, the m-th antenna will receive it with a time delay or a phase delay compared to the first antenna. The time delay would be of $(m-1)\mathrm{d}\sin(\theta)/c$ seconds and the phase delay of $(m-1)\omega_c \mathrm{d}\sin(\theta)/c$, where c is the propagation speed and ω_c is the carrier wave frequency. With this configuration, only one angle can be determined. There are other configurations, such as placing the antennas in a square array [30], which allow estimating two angles, azimuth θ_m and elevation ϕ_m, instead of just one. A target with unknown position $\boldsymbol{u} = [u_x, u_y, u_z]^T$ can send a signal to multiple receivers or observation stations with antenna arrays $\boldsymbol{s}_m = [s_{x,m}, s_{y,m}, s_{z,m}]^T$. The angles measured at the receivers with known locations provide the target's position.

$$\begin{bmatrix} \theta_m \\ \phi_m \end{bmatrix} = \begin{bmatrix} atan2(u_y - s_{y,m}, u_x - s_{x,m}) \\ atan2(u_z - s_{z,m}, \sqrt{(u_x - s_{x,m})^2 + (u_y - s_{y,m})^2}) \end{bmatrix} \tag{2.5}$$

The main sources of error in this method are the position error of the arrays, which is related to the accuracy of the GNSS receivers, and the attitude determination error of the CubeSats. This method does not need clock synchronization [1]. It is also worth noticing that the further the distance to the target, the greater the position estimation error. At least two receivers are needed to estimate the position of a target in three dimensions (3D) [59]. It is common to have more than two receivers or to combine this method with another one to improve the estimation. There have been implementations of hybrid models combining AOA with RSS [3, 5], AOA with TDOA and RSS [6], and AOA with TDOA and FDOA [32] to name a few. For this work, I will focus on AOA with TDOA. A 2D method for AOA with TDOA has been developed for wireless communication systems [27], and a 3D method in the presence of sensor errors [10]. Yin *et al.* proposed a closed-form solution method in 3D using only two receivers [33]. This method is relevant to my research since I can apply this method using two CubeSats only. I will need to consider the requirements and constraints that happen in the space environment and satellite applications.

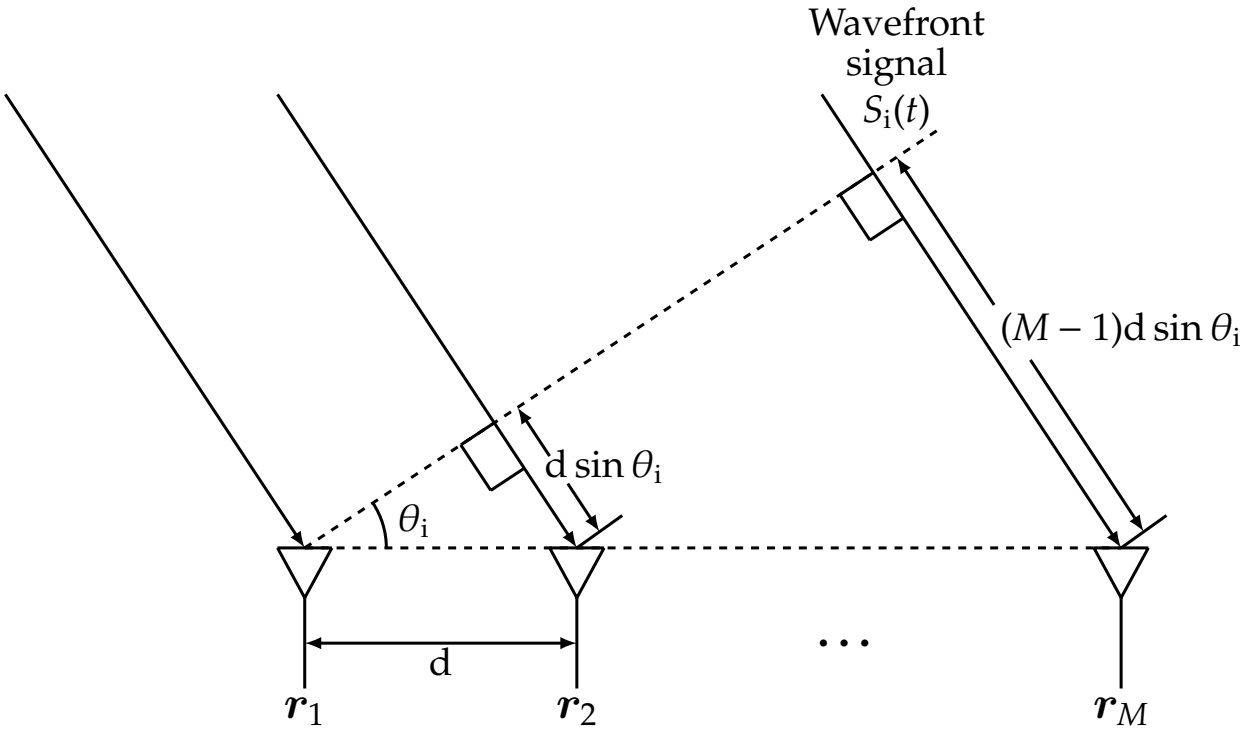

Figure 2.3: This diagram is a linear antenna array with M antennas spaced evenly at a distance of d. The signal arrives at an angle θ_i, traveling different distances to each antenna. These distances create a time delay or a phase delay between the antennas [1].

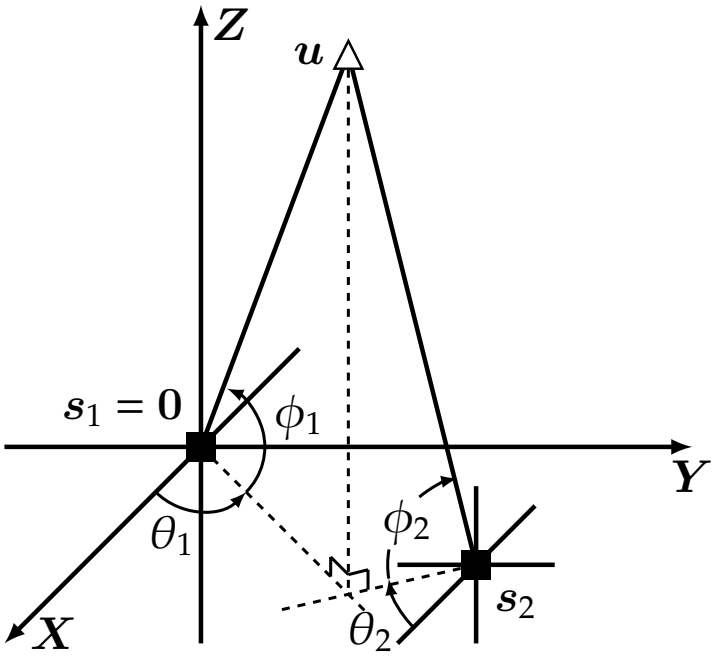

Figure 2.4: In this picture, the stations $\boldsymbol{s}_1$ and $\boldsymbol{s}_2$ receive a signal sent from the target $\boldsymbol{u}$. The stations use their antenna arrays to obtain the azimuth θ_m and elevation ϕ_m of the target.

2.3.3 A combination of AOA with TDOA

As mentioned before, the TDOA method requires four receivers with known positions to estimate the location of a target in 3D. The AOA method can estimate the target's location with just two receivers. It is common to use a third receiver or a combination of multiple methods to improve the estimation. In [60] three receivers were used to estimate the position with UWB systems. However, [33] proposed a closed-form solution method using two stations or references, combining two AOA pairs (θ_m, ϕ_m) and one TDOA. This research was intended for ground applications, using stations at fixed positions. For this reason, they simulated elevation angles of $\phi_m \in (-\pi/2, \pi/2)$ and azimuth $\theta_m \in (0, \pi/2)$. I based my work on this research because that solution can attain the Cramér-Rao bound (CRB) using only two stations and the TDOA and AOA methods. Other solutions involve at least three stations [60], or more methods than just TDOA with AOA [6, 32] or in just 2D [61].

The measurement model in vector form is:

$$\hat{\boldsymbol{\kappa}} = \boldsymbol{\kappa} + \boldsymbol{\varepsilon}, \tag{2.6}$$

where $\hat{\boldsymbol{\kappa}} = [\hat{\tau}_{2,1}, \hat{\boldsymbol{\kappa}}_1^T, \hat{\boldsymbol{\kappa}}_2^T]^T \in \mathbb{R}^5$ is the measurement vector, and the real vector is given by $\boldsymbol{\kappa} = [\tau_{2,1}, \boldsymbol{\kappa}_1^T, \boldsymbol{\kappa}_2^T]^T \in \mathbb{R}^5$ whose elements are related to the source position by equations 2.4 and 2.5, with

$$\boldsymbol{\kappa}_m = \begin{bmatrix} \theta_m \\ \phi_m \end{bmatrix}, \; m = 1, 2. \tag{2.7}$$

The localization geometry (see Fig. 2.4) shows that

$$\boldsymbol{u} - \boldsymbol{s}_m = r_m \boldsymbol{b}_m, \; m = 1, 2, \tag{2.8}$$

where $\boldsymbol{b}_m = \begin{bmatrix} \cos\phi_m \cos\theta_m, & \cos\phi_m \sin\theta_m, & \sin\phi_m \end{bmatrix}^T \in \mathbb{R}^3$ is the unit vector of the actual source location with respect to the mth station.

Let $\boldsymbol{G}_m \in \mathbb{R}^{3x2}$ be

$$\boldsymbol{G}_m = \begin{bmatrix} \sin\theta_m & \sin\phi_m \cos\theta_m \\ -\cos\theta_m & \sin\phi_m \sin\theta_m \\ 0 & -\cos\phi_m \end{bmatrix}, \; m = 1, 2. \tag{2.9}$$

Let $\boldsymbol{G} \in \mathbb{R}^{3x5}$ be

$$\boldsymbol{G} = [2(\boldsymbol{b}_2 - \boldsymbol{b}_1), \boldsymbol{G}_1, \boldsymbol{G}_2] \tag{2.10}$$

Let $\boldsymbol{h} \in \mathbb{R}^5$ be

$$\boldsymbol{h} = \left[(\boldsymbol{b}_2 - \boldsymbol{b}_1)^T(\boldsymbol{s}_1 + \boldsymbol{s}_2 - \tau_{21}\boldsymbol{b}_1), \boldsymbol{s}_1^T\boldsymbol{G}_1, \boldsymbol{s}_2^T\boldsymbol{G}_2\right]^T \tag{2.11}$$

From [33] we obtain:

$$\hat{\boldsymbol{h}} \approx \hat{\boldsymbol{G}}^T\boldsymbol{u} + \boldsymbol{T}\boldsymbol{\varepsilon}, \tag{2.12}$$

where $\hat{\boldsymbol{h}}$, $\hat{\boldsymbol{G}}$ have the measurements values,

$$\boldsymbol{T} = \begin{bmatrix} -(\boldsymbol{b}_2 - \boldsymbol{b}_1)^T\boldsymbol{b}_1 & r_1\boldsymbol{b}_2^T\boldsymbol{L}_1 & -r_2\boldsymbol{b}_1^T\boldsymbol{L}_2 \\ \boldsymbol{0}_2 & \boldsymbol{T}_1 & \boldsymbol{0}_{2x2} \\ \boldsymbol{0}_2 & \boldsymbol{0}_{2x2} & \boldsymbol{T}_2 \end{bmatrix}, \tag{2.13}$$

$$\boldsymbol{L}_m = \begin{bmatrix} -\cos\phi_m \sin\theta_m & -\sin\phi_m \cos\theta_m \\ \cos\phi_m \cos\theta_m & -\sin\phi_m \sin\theta_m \\ 0 & \cos\phi_m \end{bmatrix}, \tag{2.14}$$

$$\boldsymbol{T}_m = -r_m \begin{bmatrix} \cos\phi_m & 0 \\ 0 & 1 \end{bmatrix} \tag{2.15}$$

It follows from 2.6 that $\boldsymbol{T}\boldsymbol{\varepsilon}$ in 2.12 is zero-mean Gaussian with the covariance matrix $\boldsymbol{W} = \boldsymbol{T}\boldsymbol{Q}\boldsymbol{T}^T$. As a result, the weighted LS estimate of $\boldsymbol{u}$ is:

$$\hat{\boldsymbol{u}} = \left(\hat{\boldsymbol{G}}\boldsymbol{W}^{-1}\hat{\boldsymbol{G}}^T\right)^{-1}\hat{\boldsymbol{G}}\boldsymbol{W}^{-1}\hat{\boldsymbol{h}}^{-1} \tag{2.16}$$

The matrix $\boldsymbol{W}$ is not known in practice since it depends on the unknown position. The solution to this problem is to initiate the algorithm with $\boldsymbol{W}$ as the identity matrix and to do up to two repetitions to obtain the position estimation.

2.4 Position localization beyond the Earth

The Deep Space Network (DSN) is a network of multiple ground stations owned by the US for NASA's interplanetary missions. These ground stations are in different parts of the world. The DSN has been operational since 1963 to uplink, downlink, and track deep-space spacecraft. The number of satellites supported by the DSN has been increasing, especially small satellites. This increment in satellites makes it hard to meet the needs of all of them [62]. The following are the latest position estimation methods that do not require the aid of the DSN and can support interplanetary missions.

2.4.1 X-ray Pulsar Navigation (XNAV)

Neutron stars, called pulsars, are rotating stars with high magnetic fields that emit electromagnetic radiation through their magnetic poles. Due to their rotation and radiation emission, we see them as pulsating radio sources, similar to how the lighthouses work in visible light. The first observation of these pulsating phenomena was reported in 1964 [63] by the radio astronomer Dr. Antony Hewish. He discovered the Pulsars by chance when he was studying quasars in Cambridge [64]. Dr. Hewish said the pulses were so regular that they could be used as clocks. In 1974, Downs proposed using pulsars for interplanetary navigation [65]. In 1991, Dr. Joseph H. Taylor demonstrated that a special class of pulsars, called MilliSecond Pulsars (MSPs) have fractional stabilities comparable to those of the best atomic clocks [66]. Like in the case of stars, there is a pulsar catalog with the information of their names, positions, magnitudes, pulse frequencies, and pulse width, among other parameters [67].

The China Academy of Space Technology (CAST) designed and developed the first pulsar navigation mission called XPNAV-1. It is a 270 kg satellite launched on November 10, 2016, in LEO orbit. It successfully validated its capability of observing X-ray pulsars [68]. In June 2017 NASA installed aboard the ISS the Neutron Star Interior Composition Explorer (NICER). It is comprised of an array of 56 Silicon Drift Detectors with an effective area of 2000 cm^2 in total. This instrument provides high-precision measurements of Pulsars in the soft X-ray band. The NICER mission was enhanced with the Station Explorer for X-ray Timing and Navigation Technology (SEXTANT) technology demonstration. The goal of SEXTANT was to demonstrate real-time, on-board X-ray pulsar navigation using MSPs [69]. It collects X-ray photon events time, accurate to 100 ns (RMS). These events are processed using a Maximum Likelihood (ML) estimator, yielding estimates of pulse phase and frequency [70] which is used to calculate the position of the spacecraft. It achieved a Root-Sum-Squared (RSS) error of less than 10 km in-orbit once converged, using highly accurate timestamps from the NICER GPS receiver [71, 72]. The Insight-Hard X-ray Modulation Telescope (Insight-HXMT) satellite was launched in 2017 and conducted an in-orbit demonstration of XNAV. It used a new method called Significance Enhancement of Pulse-profile with Orbit-dynamics (SEPO) which needs only one pulsar and combines the significance analysis of the pulse profile and orbit dynamics. With this method, they obtained position estimations within 10 km (3σ) and a velocity within 10 m/s (3σ) [73].

2.4.2 Star trackers used in position estimation

Star trackers are commonly used for attitude determination. Some researchers are exploring the idea of using star trackers for position estimation. Dr. Karimi proposed an interplanetary autonomous navigation system using a star tracker pointing to visible planets with an EKF in 2015 [74]. A new weighted least-squares single-point position estimation was proposed for the same scenario in 2017 [75]. In 2021 an autonomous optical navigation system for a deep-space CubeSat mission was tested in a processor-in-the-loop simulation using a Raspberry Pi 4 model B, and an EKF [76]. Dr. Andreis proposed in 2022 a Vision-Based Navigation (VBN) system for a deep-space CubeSat mission. The studied scenario was an interplanetary trajectory leg between Earth and Mars, using multiple consecutive observations of two planets and an EKF. This simulation yielded a 3σ accuracy of

1,025 km and 0.42 m/s spacecraft position and velocity [77].

3. Theoretical framework

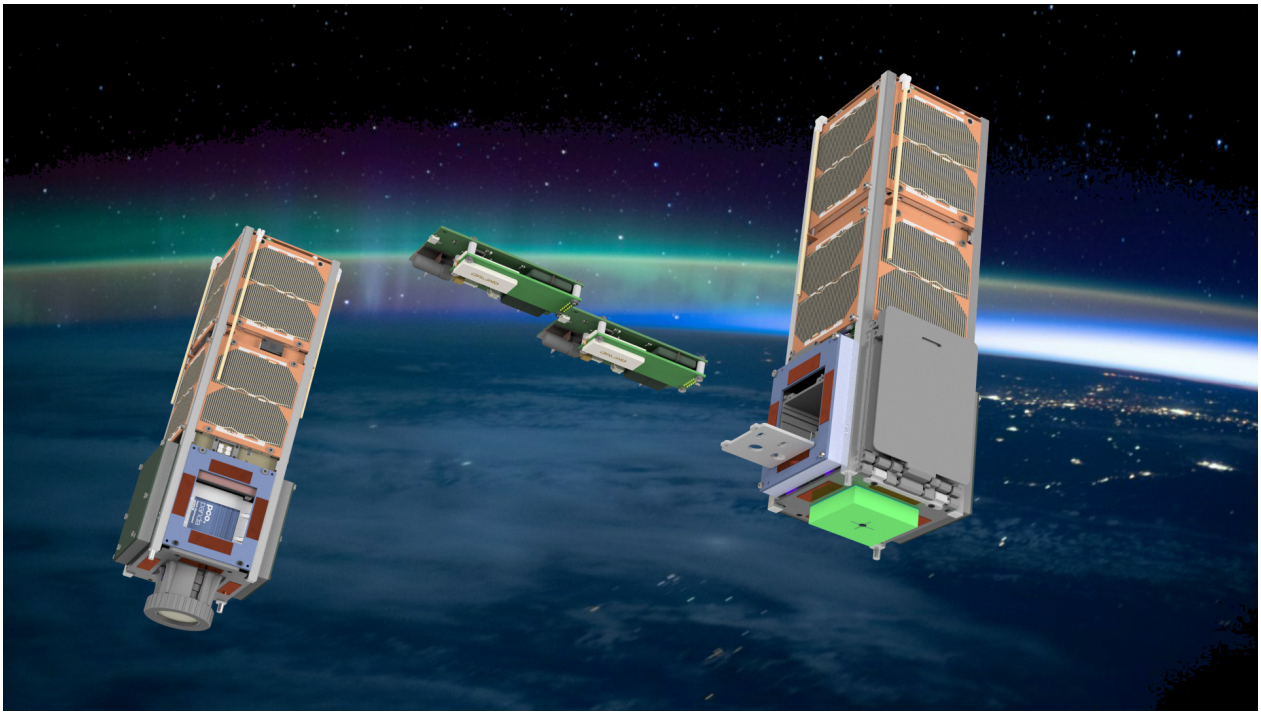

Figure 3.1: The goal of this Thesis is to evaluate the possibility of estimating the position of a femto-satellite using only two CubeSats. Although I did my research using simulations, I took elements of an actual situation. We have two CubeSats in space with Star Trackers, GNSS receivers, S-band transceivers, and antenna arrays. Most importantly, we have a Femto-satellite Orbital Deployer (FOD) with a femto-satellite on board the SUCHAI-3.

3.1 Coordinate systems

In space, just like on Earth, we need coordinate systems to determine the position of an object. These coordinate systems can be inertial or non-inertial frames. The difference between them is that an inertial frame is not accelerating. One of the inertial frames used for objects in space is the Earth-Centered Inertial (ECI) coordinate frame. This frame has its origin at the center of mass of the Earth. The $\boldsymbol{Z}$ axis of this frame is aligned with the Earth's North Pole. Its $\boldsymbol{X}$-$\boldsymbol{Y}$ plane coincides with the equatorial plane. The equatorial

plane is a great circle of an imaginary celestial sphere, and it is in the same plane as the equator of Earth. The $\boldsymbol{X}$ axis points towards the vernal equinox. The vernal equinox is the equinox on Earth when the point where the sun is at the zenith crosses the celestial equator from south to north. A non-inertial frame similar to the ECI frame is the Earth-Centered, Earth-Fixed (ECEF) coordinate system. This coordinate system rotates with the Earth at the same angular velocity, and it is useful to determine the position of objects on the Earth's surface. The GPS satellite navigation system uses this reference frame with the geodetic datum WGS 84, which approximates the Earth's shape as an ellipsoid. The Local Vertical/Local Horizontal (LVLH) frame is attached to an orbiting satellite. The x axis points in the direction of movement, the z axis points to the Nadir, and the y axis is orthogonal to them. These frames and others are useful for rendezvous [78, 79], proximity operations [80, 81], docking [82, 83], formation flying [84, 85], and satellite deployments [86, 87]. Figure 3.2 shows an LVLH frame attached to a CubeSat and an ECI frame.

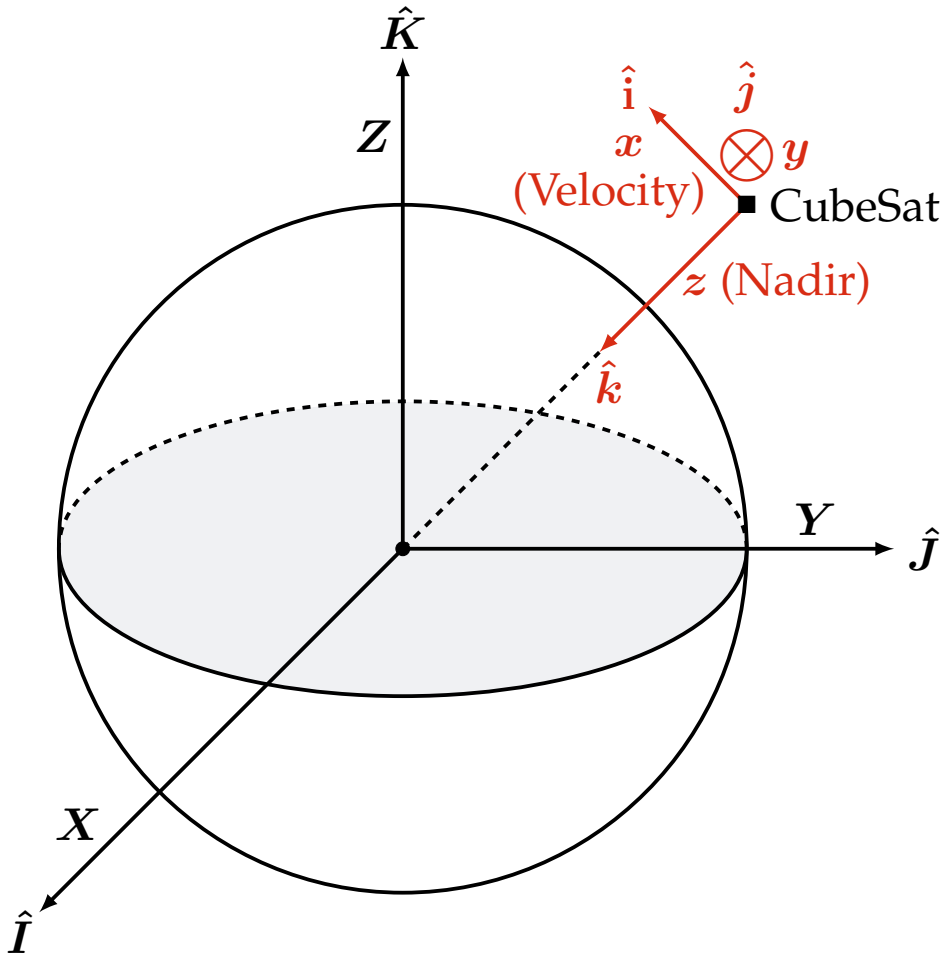

Figure 3.2: The Earth-Centered Inertial (ECI) coordinate frame, in black, has its origin at the center of mass of the Earth. It is useful to describe a satellite's position. A Local Vertical/Local Horizontal (LVLH) frame, in red, is attached to a satellite, in this case, a CubeSat. The **x** axis points towards the direction of movement, **z** to the nadir, and **y** is orthogonal to them. The LVLH frame can be used for rendezvous, docking, and satellite deployments.

3.2 Initial position estimation

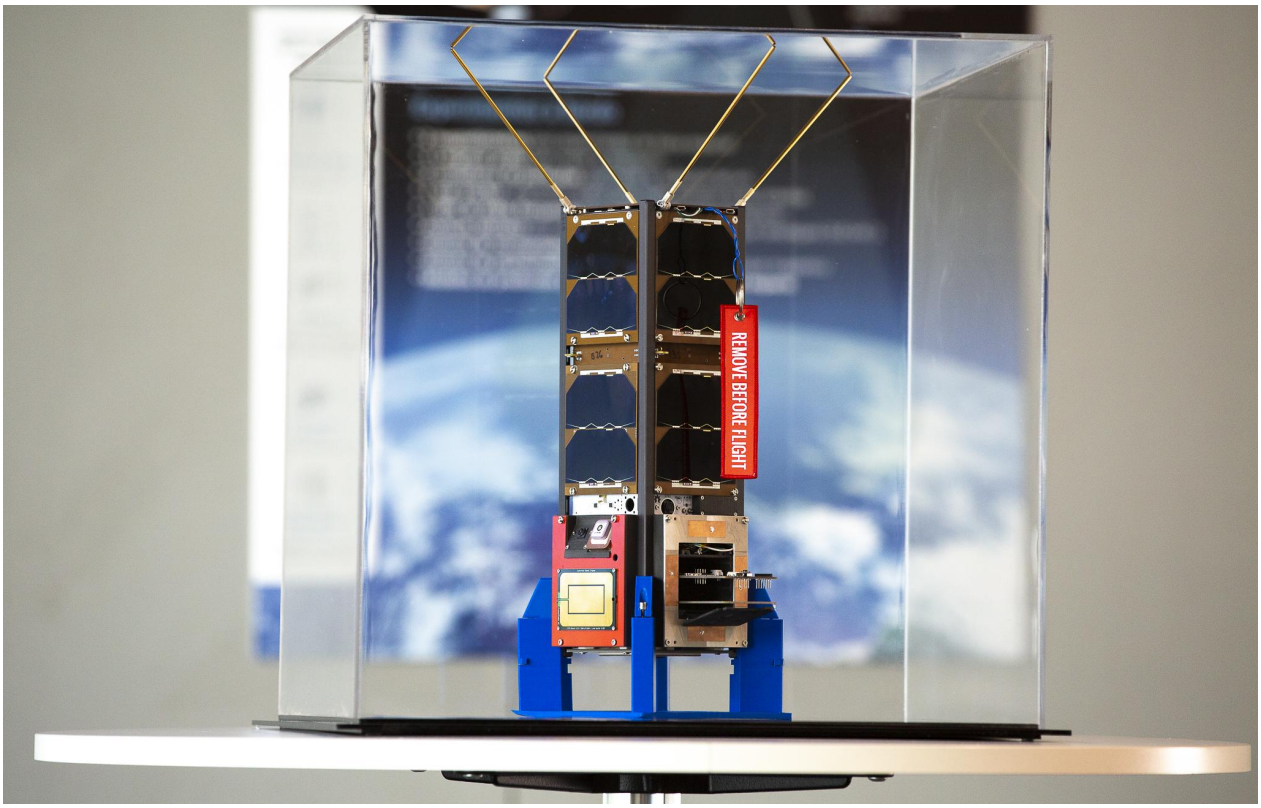

Figure 3.3: A 3U CubeSat has enough space to have femto-satellites and a deployment system for the femto-satellites. This picture shows the SUCHAI 3 carrying two femto-satellites.

CubeSats can deploy femto-satellites. One example is KickSat, a crowd-funded 3U CubeSat that carried 128 femto-satellites called Sprites [14]. Unfortunately, due to a master clock reset, the KickSat 1 could not deploy the Sprites before reentering the atmosphere [20]. However, KickSat 2 successfully deployed 105 Sprites into orbit on March 18, 2019. The deployment system that used KickSat consisted of using the nitinol wire antennas of the Sprites as springs to push them out of the CubeSat [14]. Another deployment mechanism is the Hold-Release Mechanism (HRM), based on the wire-cut system by heating [88]. The heating element cuts a cable that is holding in place, for example, solar panels, antennas, or in this case, a femto-satellite. VELOX-I, a 3U CubeSat, used a nichrome wire to cut a nylon cable to deploy its solar panels [89]. Kailaje *et al.* reported the advantages of an Ultra High Molecular Weight Polyethylene (UHMWPE or HMPE) cable, commonly used in fishing lines, over the nylon cable for an HRM on nano-satellites [90].

The Space and Planetary Exploration Laboratory (SPEL) from Universidad de Chile developed three 3U CubeSats: SUCHAI 2, SUCHAI 3, and PlantSat. One of the payloads is a Femto-satellite Orbital Deployer (FOD) designed to deploy two femto-satellites (Figure 3.3). The FOD payload uses a spring to push the femto-satellites out of SUCHAI 3. The

gate is closed using a cable tied at each end to a resistor to hold the femto-satellite in place. When the payload receives the instruction to deploy, a microcontroller polarizes a transistor, allowing the current to pass through the resistors. These resistors heat up until one of them cuts the cable, opening the gate. After this, the spring pushes the femto-satellite through a rail into orbit. This rail gives stability to the femto-satellite to deploy it in the desired direction.

One of the advantages of deploying a femto-satellite from our CubeSat is that we can have an initial estimation of the femto-satellite's position and velocity. Since the CubeSat has a GNSS device, we can obtain its position and velocity. The CubeSat can also have an attitude determination system, such as a star tracker, to know its orientation [91]. If we also know the speed at which the femto-satellite is deployed from the CubeSat, then we can combine this information to obtain the femto-satellite's initial position and velocity in the CubeSat's LVLH frame. This first estimation is not only useful for my algorithm but it can also be used to calculate the femto-satellite's orbital elements.

To calculate the orbital elements of the femto-satellite, we need to transform the position and velocity vectors from the CubeSat's LVLH frame to the perifocal frame, and from the perifocal frame to the ECI frame. After this, the procedure is well known and can be found in the literature [2]. The CubeSat can send these orbital elements to a ground station. With this data, the femto-satellite can be found in case it has any system failure. This data can also be used as input for a dynamic model of the orbit.

3.3 Hill–Clohessy–Wiltshire dynamic model

In many ground-based applications, the movement of a target is random. For example, when the target is a Mobile Station (MS) on a cellular network. However, the trajectory of a satellite follows an orbit. This orbit is *a priori* information that I can use to improve the position estimation of the satellite. The orbit changes over time due to space weather conditions, atmospheric drag on Low Earth Orbit (LEO), and electromagnetic drag (if the satellite uses an electromagnetic tether), among other reasons. Because of these changes, regular measurements using range-based and angle-based localization systems are needed to correct the model.

Hill–Clohessy–Wiltshire (HCW) dynamic model [92] describes the relative orbit motion of a target or deputy from the perspective of a chaser or chief. It uses the LVLH frame as seen in Figure 3.2. It is common to simplify the equations assuming the chief is in a circular orbit. The mean motion of the chief satellite is $n = \sqrt{\mu/r_c^3}$, where μ is Earth's standard gravitational parameter, and r_c is the current orbit radius of the chief satellite. The HCW dynamic model is used in spacecraft formation and rendezvous planning. In this model, the target's position and velocity are given by

$$\boldsymbol{x} = \left[\boldsymbol{\rho}^T \ \dot{\boldsymbol{\rho}}^T\right]^T \in \mathbb{R}^6, \tag{3.1}$$

where $\boldsymbol{\rho} = [x, y, z]^T$ is the position of the target from the chaser's LVLH frame. The

Taylor series expansion of the two-body orbit dynamic model can be truncated in different orders to obtain different models. [93] used these equations with an EKF, and demonstrated that higher-order nonlinear dynamic models increase the observability and improve the performance of the EKF. In the next equations, $\boldsymbol{r}_c = [0, 0, -r_c]^T$ and $\boldsymbol{r}_\mathrm{d} = [x, y, z - r_c]^T$ are the positions of the chief and the deputy with respect to the center of the Earth, expressed in the chief's LVLH frame.

3.3.1 Full nonlinear dynamic model

$$\boldsymbol{f}(\boldsymbol{x}) = \begin{bmatrix} 0_{3x3} & \boldsymbol{I}_{3x3} \\ -\tilde{\boldsymbol{\omega}}^2 & -2\tilde{\boldsymbol{\omega}} \end{bmatrix} \begin{bmatrix} \boldsymbol{\rho} \\ \dot{\boldsymbol{\rho}} \end{bmatrix} + \begin{bmatrix} 0_{3x1} \\ -\tilde{\boldsymbol{\omega}}^2 \boldsymbol{r}_c - \frac{\mu}{\|\boldsymbol{r}_\mathrm{d}\|^3} \boldsymbol{r}_\mathrm{d} \end{bmatrix} \tag{3.2}$$

Where $\tilde{\boldsymbol{\omega}}$ is a skew-symmetric matrix defined by

$$\tilde{\boldsymbol{\omega}} = \begin{bmatrix} 0 & 0 & n \\ 0 & 0 & 0 \\ -n & 0 & 0 \end{bmatrix} \tag{3.3}$$

3.3.2 First-order dynamic model

This model is one of the most known versions of the HCW dynamic model, and it is defined by the following equation

$$\boldsymbol{f}(\boldsymbol{x}) = \begin{bmatrix} 0_{3x3} & \boldsymbol{I}_{3x3} \\ \boldsymbol{K} & -2\tilde{\boldsymbol{\omega}} \end{bmatrix} \begin{bmatrix} \boldsymbol{\rho} \\ \dot{\boldsymbol{\rho}} \end{bmatrix} \tag{3.4}$$

where the matrix $\boldsymbol{K}$ is given by

$$\boldsymbol{K} = \begin{bmatrix} 0 & 0 & 0 \\ 0 & -n^2 & 0 \\ 0 & 0 & 3n^2 \end{bmatrix} \tag{3.5}$$

3.3.3 Second-order dynamic model

This model adds second-order terms of the Taylor series to the previous model. All the second-order terms are inside the matrix $\boldsymbol{\Gamma}_2(\boldsymbol{\rho})$ defined in equation 3.7.

$$\boldsymbol{f}(\boldsymbol{x}) = \begin{bmatrix} 0_{3x3} & \boldsymbol{I}_{3x3} \\ \boldsymbol{K} & -2\tilde{\boldsymbol{\omega}} \end{bmatrix} \begin{bmatrix} \boldsymbol{\rho} \\ \dot{\boldsymbol{\rho}} \end{bmatrix} + \begin{bmatrix} 0_{3x1} \\ \boldsymbol{\Gamma}_2(\boldsymbol{\rho}) \end{bmatrix} \tag{3.6}$$

$$\boldsymbol{\Gamma}_2(\boldsymbol{\rho}) = \frac{\mu}{\boldsymbol{r}_c^4} \begin{bmatrix} \frac{3}{2}x^2 + \frac{3}{2}y^2 - 3z^2 \\ -3xz \\ 3yz \end{bmatrix} \tag{3.7}$$

3.3.4 Third-order dynamic model

This model is similar to the second-order dynamic model, but it also includes the third-order terms of the Taylor expansion, which are contained in the matrix $\mathbf{\Gamma}_3(\boldsymbol{\rho})$ given by the equation 3.9.

$$\boldsymbol{f}(\boldsymbol{x}) = \begin{bmatrix} 0_{3x3} & \boldsymbol{I}_{3x3} \\ \boldsymbol{K} & -2\tilde{\boldsymbol{\omega}} \end{bmatrix} \begin{bmatrix} \boldsymbol{\rho} \\ \dot{\boldsymbol{\rho}} \end{bmatrix} + \begin{bmatrix} 0_{3x1} \\ \mathbf{\Gamma}_2(\boldsymbol{\rho}) + \mathbf{\Gamma}_3(\boldsymbol{\rho}) \end{bmatrix} \tag{3.8}$$

$$\mathbf{\Gamma}_3(\boldsymbol{\rho}) = \frac{\mu}{\boldsymbol{r}_c^5} \begin{bmatrix} -4z^3 + 6z(x^2 + y^2) \\ -6xz^2 + \frac{3}{2}x^3 + \frac{3}{2}xy^2 \\ 6yz^2 - \frac{3}{2}y^3 - \frac{3}{2}yx^2 \end{bmatrix} \tag{3.9}$$

3.4 Characteristics and classification of a localization system

The localization systems can be classified in the following ways [7]:

- Centralized or distributed: A centralized system consists of one fusion center collecting all the data and computing the location of each target. A distributed approach would be for each target to estimate its position, or a nearby Base Station (BS). In the context of a femto-satellite ad-hoc constellation, a centralized system would require to transmit all the data into the main satellite, or a ground station. The result would not be in real-time, but the sensor data can be associated with their respective time and place. A distributed system, however, would be in real-time, scalable, and limited to the femto-satellite's computing power. In my application, the CubeSats collect the AOA and TDOA data of the femto-satellite and relay this data to the ground station. Therefore, this localization system is centralized.
- Non-cooperative or cooperative: If the localization system is non-cooperative, the targets estimate their position using only the BS data, in this case, the CubeSat's data. If the system is cooperative, the targets can communicate with each other to further improve the accuracy of the estimation. For this thesis, I focus on a non-cooperative system.
- Deterministic or probabilistic: A probabilistic localization system uses *a priori* information, while a deterministic system does not. I simulated a deterministic localization system using only the measurement data provided by CubeSat's clock and antenna arrays. I also used the HCW dynamic model to test if it could improve the position estimation in certain moments when the measurements could not give an accurate estimation. This model is not fused with the measurements, therefore, it is still deterministic.

3.5 Quality parameters

Hofmann *et al.* [94] described the key statistic quality parameters to determine the performance of a localization system. They were based on the 2005 US Federal Radionavigation Plan (Department of Defense *et al.* 2005: Appendix A).

- Accuracy: Accuracy is a measure of how correct is an estimation or measurement compared to the true value.
- Availability: The percentage of time the localization system can operate under its nominal parameters. For my application, the availability is directly related to the Line-Of-Sight (LOS) between the satellites, which can be obstructed by Earth. In Figure 3.4 we can see an example [2] for two satellites, A and B, orbiting a planet C of radius R. The threshold angle to determine if there is LOS or not can be obtained with the position vectors using the equation 3.10. The angles formed from the center O to the tangential points T_1 and T_2 and from the center O to the satellites A and B can be calculated using the equation 3.11.

$$\theta = \cos^{-1}\left(\frac{\mathbf{r_A} \cdot \mathbf{r_B}}{r_A r_B}\right) \tag{3.10}$$

$$\theta_1 = \cos^{-1}\left(\frac{R}{r_A}\right) \qquad \theta_2 = \cos^{-1}\left(\frac{R}{r_B}\right) \tag{3.11}$$

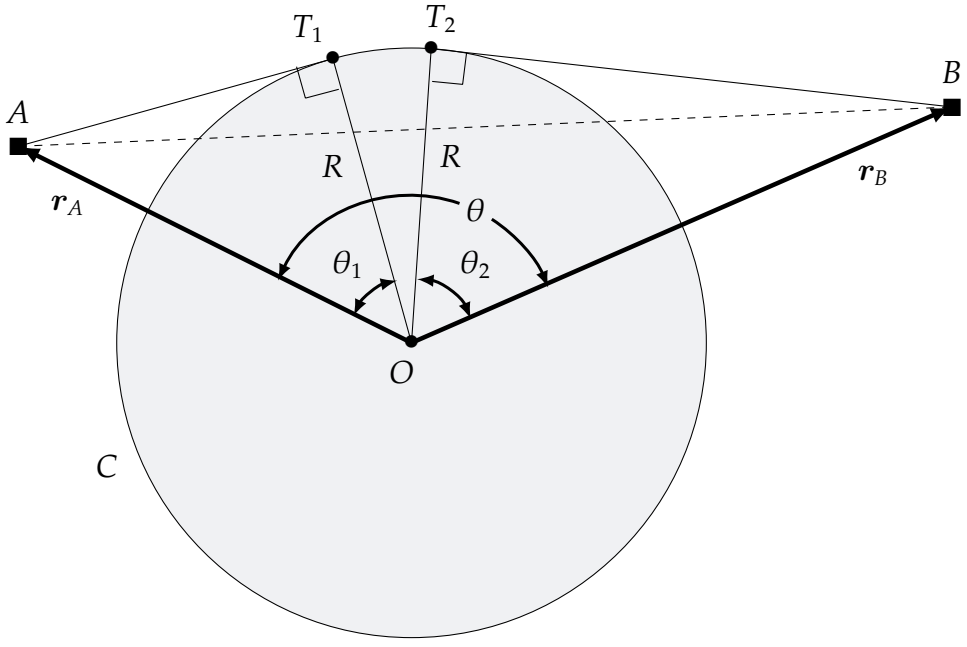

Figure 3.4: Example to know if two bodies have LOS or are interrupted by the Earth [2]. If $\theta_1 + \theta_2 < \theta$, there is NLOS. Else, if $\theta_1 + \theta_2 \geq \theta$, there is LOS.

- Capacity: The number of targets that can obtain their position simultaneously using this localization system.

- Continuity: It is the probability that the localization system will perform uninterrupted throughout a scheduled operation.
- Coverage: The coverage of a localization system is the space volume where a target can be located within a certain level of accuracy.
- Integrity: It is the ability to raise an alarm if the position error is above a certain threshold to warn the target that the position estimation should be rejected.

4. Methodology

The purpose of this thesis is to implement a localization system to estimate the position of a femto-satellite. This implementation is in the context of the Space and Planetary Exploration Laboratory (SPEL) at the University of Chile. In this laboratory, we developed two 3U CubeSats (SUCHAI-2 and SUCHAI-3) equipped with GNSS receivers, Attitude Determination and Control Systems (ADCS), antenna arrays, and S-band transceivers. I also developed a femto-satellite (see Figure 1.3), which is inside the SUCHAI-3. For this reason, my implementation has to simulate only two CubeSats to estimate the position of the femto-satellite. The restriction of using only two CubeSats has its challenges, but it will also be useful for universities and research centers that do not have the budget to have a constellation of CubeSats but can afford to have multiple femto-satellites.

4.1 Tools and equations

I implemented in Python a combination of TDOA with AOA based on [33]. This implementation considers one femto-satellite and two CubeSats, all of them moving in their respective orbits. It also includes several simulations of deployment scenarios of the femto-satellite from one of the CubeSats in different directions, and in different positions in the orbit of the mother-CubeSat, at 1 m/s. With these simulations, I can find the scenario that yields the best performance for the localization methods that I am using. I also developed a Graphical User Interface (GUI) called Pypredict to display satellite orbits and their position data. In figure 4.1 there is a screenshot of Pypredict where it shows some satellites with their position using the SGP4 model, the ground track of the SUCHAI-1, the coverage of the satellites, the day/night terminator, and buttons to interact with the software.

Table 4.1: This is the Two-Line Element set (TLE) of the *FLOCK 4P-1* that I used to simulate two 3U CubeSats. To separate the CubeSats, I used an epoch difference of four seconds, equivalent to around 30 km of distance.

1	44814U	19081L	20321.73053029	.00001305	00000-0	63025-4	0 9996
2	44814	97.4788	21.6285	0013387	80.2501	280.0246	15.20374749 54001

For the simulations, I used as an example the TLE data of a 3U CubeSat from Planet Labs called *FLOCK 4P-1* (Table 4.1) that is in LEO orbit. This CubeSat has an inclination of 97.4788°, a RAAN of 21.6285°, an eccentricity of 0.0013387, an argument of the perigee

of 80.2501°, a mean anomaly of 280.0246°, and a mean motion of 15.20374749 revolutions per day. I assumed that there are two CubeSats in the same orbit, one after the other. This is common for small CubeSat constellations since they are deployed from the same rocket. For this reason, I generated two CubeSats using the same TLE at two different time epochs, with a time-lapse of four seconds (around 30 km of separation). The CubeSat-1, or mother-CubeSat, is the one that deploys the femto-satellite and is behind the second CubeSat. The deployment considers a femto-satellite of 80 g and two CubeSats of 3.2 kg each. The simulation was made for an orbit of 17 November 2020, before the satellites arrive at the South Atlantic Anomaly. I propagated all the orbits using the SGP4 model [34].

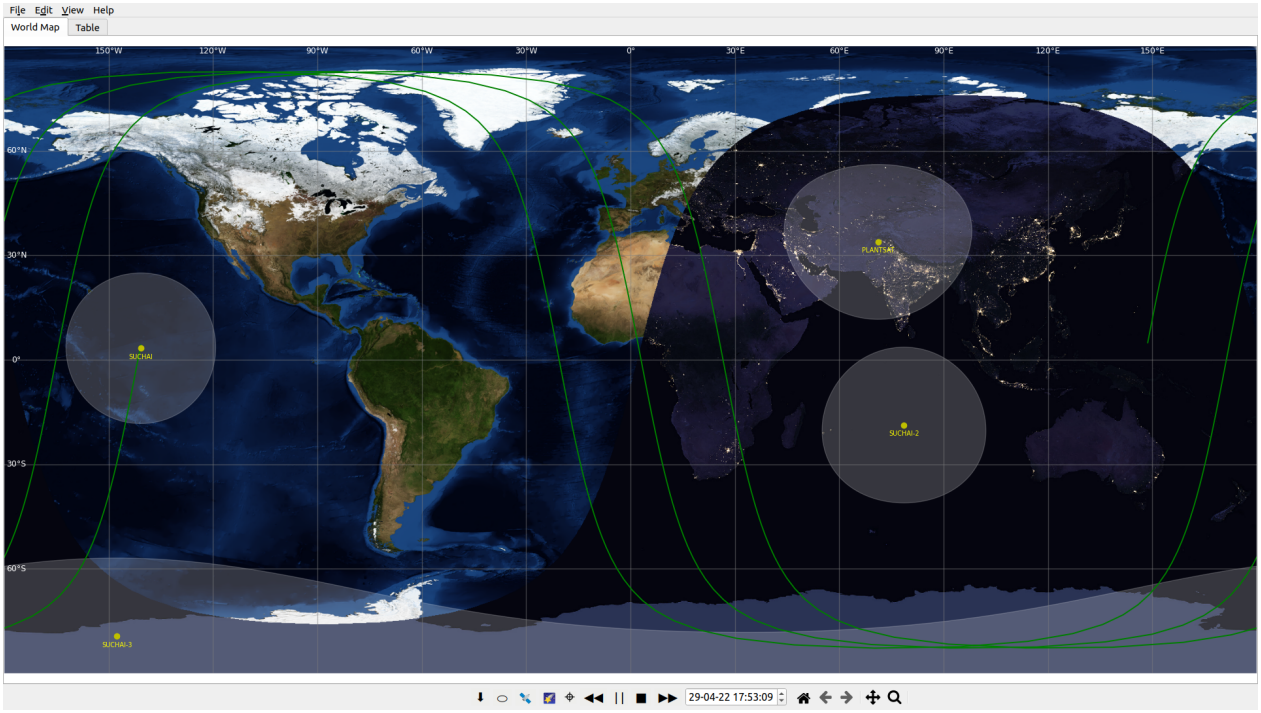

Figure 4.1: For this work, I developed a simulation platform called Pypredict. It is based on Gpredict, and it is open source. I can propagate orbits using the SGP4 model, simulate deployments of one satellite from another, display the satellite coverage and the day/night terminator, set a specific time, and fast forward and backward time, among other features.

I use the Earth-Centered Inertial (ECI) coordinate frame for calculating the satellite's positions. The femto-satellite's unknown position is represented by the vector $\mathbf{u} = \left[u_x, u_y, u_z\right]^T \in \mathbb{R}^3$ while the CubeSats are at known positions $\mathbf{s}_m = \left[s_{x,m}, s_{y,m}, s_{z,m}\right]^T \in \mathbb{R}^3$, $m = 1, 2$. The measurement of the CubeSat's position is affected by the accuracy of their GNSS device, as seen in

$$\hat{\mathbf{s}}_m = \mathbf{s}_m + \varepsilon_{m,\text{GNSS}}, \; m = 1, 2, \tag{4.1}$$

where $\varepsilon_{m,\text{GNSS}}$ is a zero-mean Gaussian noise to model the accuracy of the GNSS device. The accuracy of each axis is equal to the overall accuracy divided by $\sqrt{3}$. I use the same

measurement model as in [33] with one TDOA and two AOA pairs (θ_m, ϕ_m), but the elevation is $\phi_m \in (-\pi/2, \pi/2)$ because we are not limited to the ground. These angles correspond to each CubeSat's Local Vertical/Local Horizontal (LVLH) frame. This frame is depicted in Figure 3.2.

There are five design parameters for this localization system: the deployment direction and speed, the point in the orbit where the deployment takes place, the accuracy of the attitude determination and control systems (ADCS), and the GNSS devices of the CubeSats. For this research, I assume a speed of deployment of 1 m/s to focus on the rest of the design parameters.

I use the LVLH frame of the CubeSat with the Femto-satellite Orbital Deployer (FOD) to conduct the deployment simulations. Figure 3.2 illustrates the reference frame attached to the CubeSat. Different deployment directions and orbit's point of deployment change the localization geometry. The geometry is directly related to the performance of the localization system. Due to the limitations of the ADCS, the femto-satellite's deployment will not be in the desired direction with exactitude. The model of the deployment direction is

$$\begin{bmatrix} \hat{\theta}_{m,\text{dep}} \\ \hat{\phi}_{m,\text{dep}} \end{bmatrix} = \begin{bmatrix} \theta_{m,\text{dep}} \\ \phi_{m,\text{dep}} \end{bmatrix} + \begin{bmatrix} \varepsilon_\theta \\ \varepsilon_\phi \end{bmatrix}, \; m = 1, 2, \tag{4.2}$$

where $\theta_{m,\text{dep}}$ and $\phi_{m,\text{dep}}$ represent the yaw (azimuth) and pitch (elevation) of the deployment from the CubeSat's LVLH frame, and $\left[\varepsilon_\theta, \varepsilon_\phi\right]^T$ are zero-mean Gaussian noises for the yaw and pitch. I do this to represent the accuracy of the attitude determination system (ADS) and the attitude control system (ACS), with a variance of $\sigma^2_{\text{ADS}} + \sigma^2_{\text{ACS}}$. These values move the deployment direction from the one intended, changing the localization geometry.

With the speed and direction of deployment, I calculate the new velocities for the femto-satellite and the CubeSat that deploys it. I do this using the law of conservation of momentum. After obtaining the satellites' position and velocity, I search for the TLE set that best describes these two vectors, starting from the original TLE file of the mother-CubeSat. For this purpose, I need to find the new inclination, RAAN, eccentricity, the argument of the perigee, mean anomaly, and mean motion. Since having six nested *for* loops takes too much time, I decided to select different groups of two to three orbital elements and search for the best fit iteratively. The ballistic coefficient, B^*, and the first and second derivatives of the mean motion, $\dot{n}$, and $\ddot{n}$, respectively, are set equal to the one provided by the TLE file. This approach does not impact the prediction accuracy for short-term orbit propagations, as seen in [53]. After searching for the TLE set that better fits the position and the new velocity for each of them, I calculated a distance error below 6 m and a speed error of fewer than 0.007 m/s between the theoretical one and the one provided by the new TLE set.

The ground truth of the femto-satellite position is the SGP4 model with the TLE set obtained after simulating the femto-satellite deployment. The simulations are three days after the deployment, for a time frame of 100 min. I evaluate three days after the de-

ployment because the mission operation proposes to deploy the femto-satellite after the beginning of a strong geomagnetic storm to study the magnetic variations at several points. The duration of effects of the geomagnetic storm lasts a couple of days based on historical data [23]. I simulated a period of 100 min to guarantee the study of a complete orbit, which is around 94.5 min. I also wanted to calculate the performance for the worst-case scenario. There is a reduction in performance as the satellites separate over time. That is why I also evaluate at the end of three days.

The methodology for finding the best localization scenario is as follows. First, I simulate the deployment of the femto-satellite into different directions at 1 m/s. I compare them using the root Cramér–Rao Bound (CRB), which is statistically the lower limit of the error in the position estimation. This bound is different according to the geometry formed by the satellites and the methods used for the position estimation. If the estimator attains the root CRB, then the lowest possible error is determined by this bound. For this reason, I use this parameter to select the direction of deployment that yields the lowest root CRB. Then I evaluate if there is any difference in which point of the mother-CubeSat's orbit I deploy the femto-satellite. After selecting these values, I study how the attitude determination and the attitude control systems' accuracy affect the position estimation's performance. I choose the accuracy of these systems based on the results and on the technology that is currently available. I also simulate GNSS devices with different accuracies for the CubeSats positions. With the results of the simulations, I choose the accuracy of a GNSS receiver based on what is on the market for space applications. Finally, I evaluate this localization system using the root CRB, the Root Mean Square Error (RMSE), and the estimation bias.

The second part of my simulations consists of improving the position estimation for the worst-case scenario. In this scenario, I test if I can improve the position estimation using the HCW dynamic model instead of the measurement. I use the Runge–Kutta 4th order method to solve the differential equation 3.2. I tested multiple time steps for this method using the femto-satellite's position without noise as the initial state and iterated until ten minutes after to see the results. I selected a time step of 0.01 seconds because it was the best compromise between time and performance. To decide when to use the model, I use the distance between the femto-satellite's estimated position and the mother-CubeSat's GNSS position. I measure this distance every second. If the difference between the previous distance and the next (see equation 4.3) increases over one kilometer, then it means that the estimation error is too high. When this difference peaks, I use it to implement a time window in which I trust the model over the measurements. To obtain this time window, I tested different durations until I got a result that could remove the error peaks.

$$\Delta\text{dist}(t) = \frac{1}{L}\sum_{l=1}^{L} \text{abs}\left(\|\mathbf{u}(t) - \mathbf{s}_1(t)\| - \|\mathbf{u}(t-1) - \mathbf{s}_1(t-1)\|\right) \tag{4.3}$$

4.2 Attitude Determination and Control System (ADCS)

In the previous sections, we discussed how to determine the position of a satellite. This section is about how to obtain the spacecraft's orientation, which is called attitude, and

how to control it. On the ground, we need reference points to know where we are looking, like the mountains and hills, the coast, and a skyscraper, among others. In the space, we need other reference points. We can use sun sensors like Fine Sun Sensors (FSS) and Coarse Sun Sensors (CSS) to measure the angle of the incident light of the sun to the sensor. We can use the Earth with an Earth Sensor or a horizon sensor, using an infrared sensor or a camera. There are also other sensors like gyroscopes, accelerometers, and magnetometers, usually combined into a single Inertial Measurement Unit (IMU). The most precise sensor for attitude determination is the Star Sensor, also called Star Tracker. This sensor takes a picture of the stars and compares them with an onboard star catalog until it finds the best pattern match. For our CubeSats, we used FSS and CSS from the company GomSpace, gyroscopes, PNI RM3100 magnetometers, and a Star Sensor developed by Samuel Gutiérrez [91], based on a Raspberry Pi with a camera. With his help on the software part, I developed a second Star Sensor for both the SUCHAI-2 and SUCHAI-3. Figure 4.2 shows the PCB that integrates this camera into the satellite, and Figure 4.3 shows this PCB mounted in the SUCHAI-3.

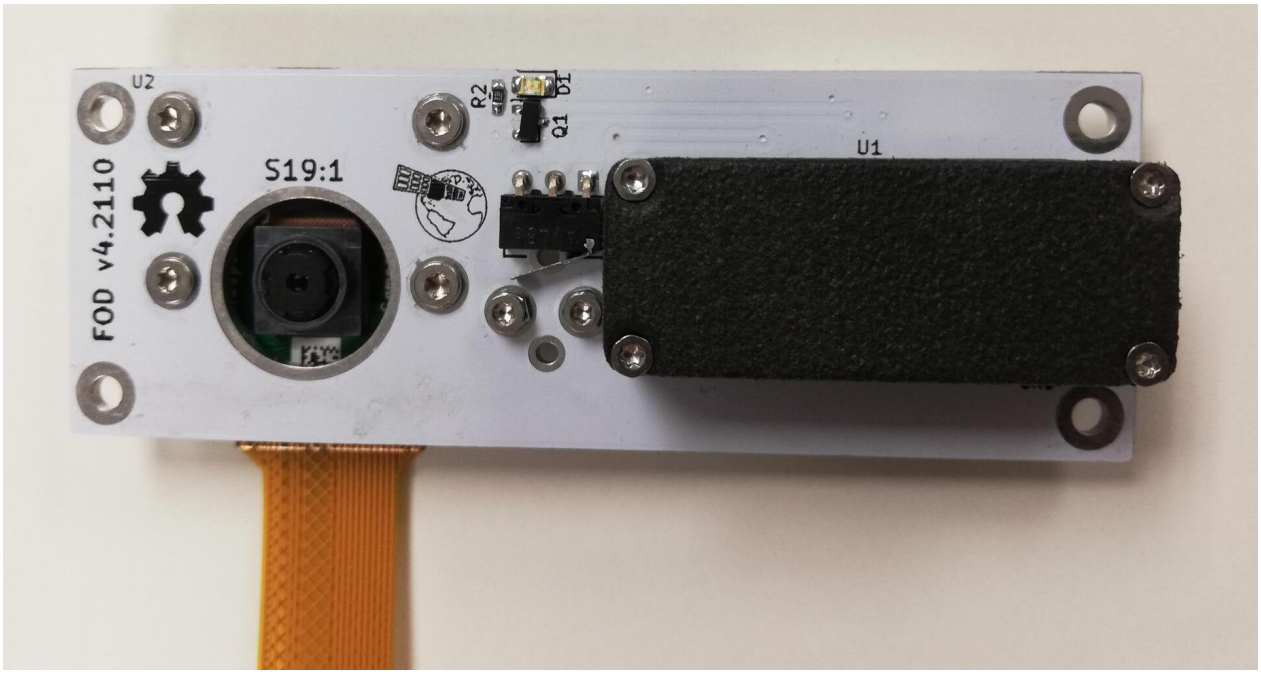

Figure 4.2: This picture shows a PCB I designed for the SUCHAI-2 and SUCHAI-3. On the left there is a Raspberry Pi camera for the second Star Sensor, in the middle there is a LED that turns on during the deployment attempt of the femto-satellite, and below the LED there is a MOSFET that allows the current to pass through the release mechanism. Bellow the MOSFET there is a switch to measure the deployment status, but it was not used in this mission, and on the right side, it has an S-band transceiver to send commands to and receive data from the femto-satellite. On the bottom side of the PCB, there is a Molex Picoblade connector for the interface between this board and the PCB that has a Raspberry Pi Zero. The Camera can be used as a second Star Sensor, and also to take pictures and/or videos of the deployment of the femto-satellite.

The three most common ways to change the attitude of a spacecraft are by using Reaction Wheels (RW), Magnetic Torquer Coils (MTC), or Thrusters. The RWs work under the principle of conservation of angular momentum. When a wheel spins in one direction, the spacecraft rotates in the opposite direction. With three wheels we can control the attitude of the satellite in the three axes. Some RWs have four wheels for redundancy in case one of the wheels fails. The MTC, also known as Magnetorquer, creates a magnetic dipole using its electromagnetic coils. This produces a torque with the planet's magnetic field and changes the satellite's attitude. When the stored momentum of an RW exceeds its maximum speed, we can use the MTC to desaturate it. Thrusters are used for attitude control, orbit maneuvers, and docking, and they work by ejecting a propellant. SPEL's CubeSats have MTC from GomSpace and RWs designed by Gustavo Díaz [95], a member of the laboratory. Figure 4.3 shows the SUCHAI-3 in one of the latest phases of the integration process, and one of the wheels can be seen from that perspective.

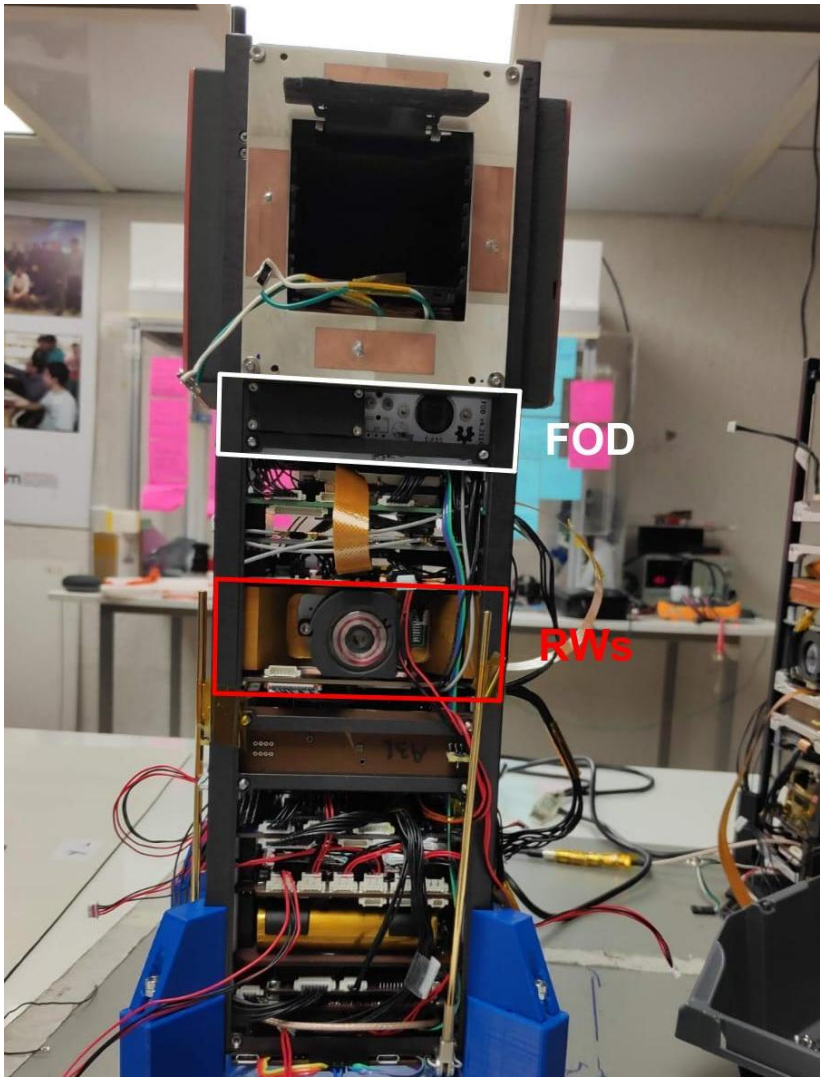

Figure 4.3: This picture is of the SUCHAI-3. Bellow the antenna array and the chamber of the femto-satellite, there is a white PCB with the electronics for the Femto-satellite Orbital Deployer (FOD) and the Raspberry Pi camera. The RW is inside the red box. Only one of the wheels is visible from that side.

Figure 4.4: This picture was taken with the camera that is mounted on the SUCHAI-3's FOD board I developed. This demonstrates that part of the electronics that are used for the femto-satellite deployment is working.

4.3 Satellite reprogramming

In SPEL we developed the flight software of our nano-satellites. This software is modular and extensible [96], and we tested it with fuzz testing techniques [97]. It runs not only on the OBC of every satellite but also inside the payloads and on the ground station. It is made in such a way, that it is easy to include new commands without changing its core or the software of other payloads. This software has the capability to send and receive files

of any type and size. It divides the files into parts and sends them to the desired node. This node can be another satellite or the ground station. The receiver can tell which parts are missing. When it has all the file parts, it can merge them and obtain the original file.

Our flight software supports the Raspberry Pi computer, therefore it supports Linux. Some of the payloads use commands that execute Python or C++ scripts. I developed commands to turn on and off some subsystems of the Raspberry Pi, and commands for taking pictures and videos, among others. The most important command I made enables the flight software to execute Linux commands and send the output to another node. It is done by using a C function called *popen*. With this command, I can make, move, copy, and rename files, ask for a payload to send to the ground station the content inside a file, ask for the total memory available, and other functions. I can upload new Python or C++ scripts to replace the current ones, and I can even recompile the entire flight software. This allows me to test new position estimation algorithms without the need to launch a new satellite. I tested all these options on Earth before the launch, and we will test them again after we execute all the experiments on board the satellites.

5. Simulation results

5.1 Localizing a femto-satellite with TDOA and AOA

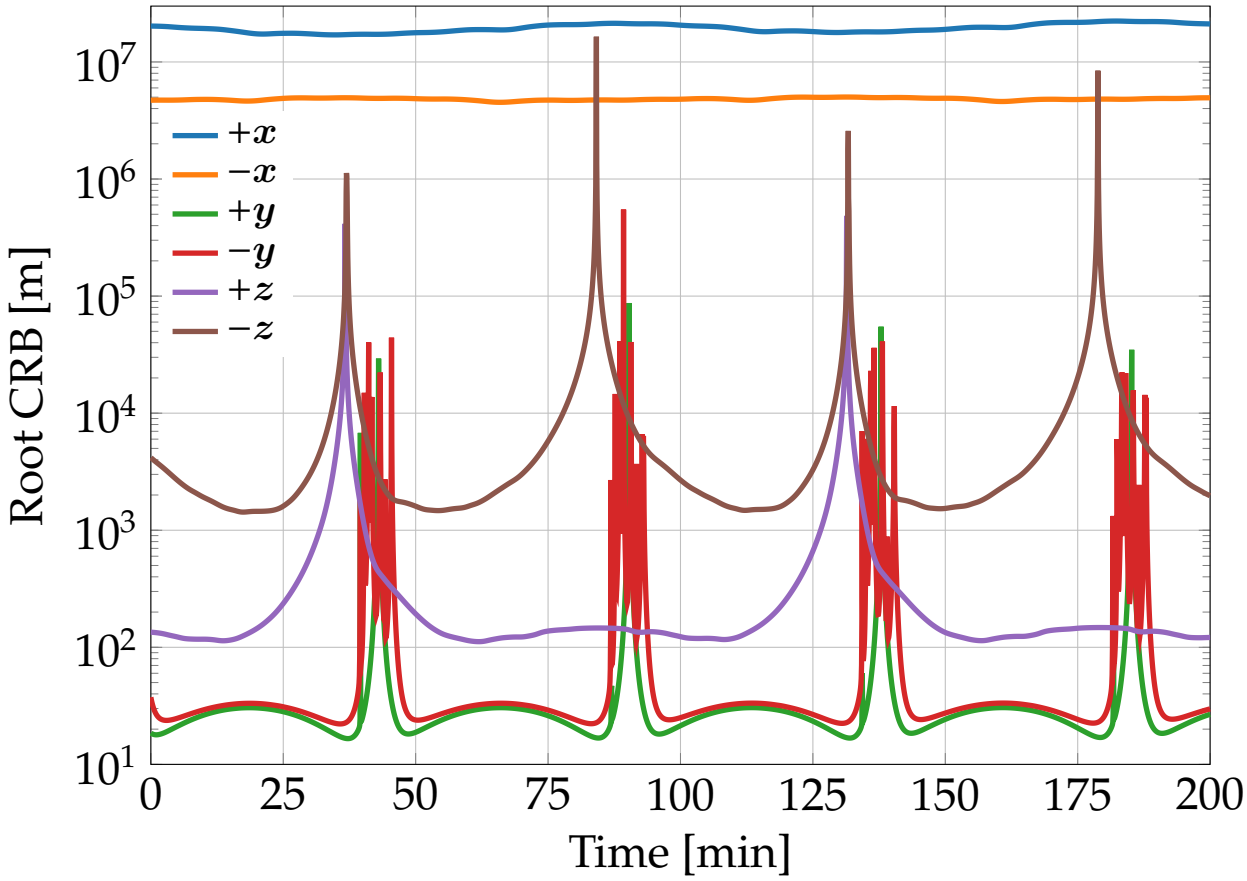

Figure 5.1: The root CRB indicates the best possible accuracy of the position estimator, and I used it to compare the six deployment directions. This figure shows the root CRB three days after the deployment of the femto-satellite at 1 m/s. The orbit's period is around 94.5 min. Each of the lines represents one of the six directions of deployment using the mother-CubeSat's LVLH frame, and it is the average of 10 different deployment points of the orbit.

$$\text{RCRB} = \sqrt{\frac{1}{L_0}\sum_{l_0=1}^{L_0} tr\,(\mathbf{MSE})} \tag{5.1}$$

I searched for the best localization scenario, assuming an ADCS with perfect accuracy. For this purpose, I simulated the deployment in the positive and negative direction of the three axes of the mother-CubeSat's LVLH frame. The **x** axis is in the direction of movement, the **z** axis points at the nadir, and the **y** axis is orthogonal to them. I selected ten orbit positions to deploy the femto-satellite, with a time step of ten minutes since the apogee. Then, I calculated the average of the root CRB for these ten scenarios. For the root CRB, I used the square root of the trace of the MSE matrix [33]. The root CRB indicates the best possible accuracy of the position estimator.

Figure 5.1 shows the root CRB for the six directions. The worst scenario is when the femto-satellite is launched on the **x** axis because it aligns with both CubeSats. The AOA method's performance decreases when there is an alignment between the target and the receivers. I obtained the best results when the deployment was made in the **y** axis because the geometry is closer to the optimal for the AOA [59]. The positive direction has lower peaks than the negative one, so I chose that one.

Now that I have chosen the deployment speed and direction, I need to find the orbit's point to deploy the femto-satellite. Figure 5.2 shows different deployment points in the same orbit towards the positive **y** axis. Highly elliptical orbits, like Molniya, are more affected by this parameter than this simulated orbit. Still, there are some variations between cases. The lowest average root CRB occurs when the deployment is 10 min after the apogee.

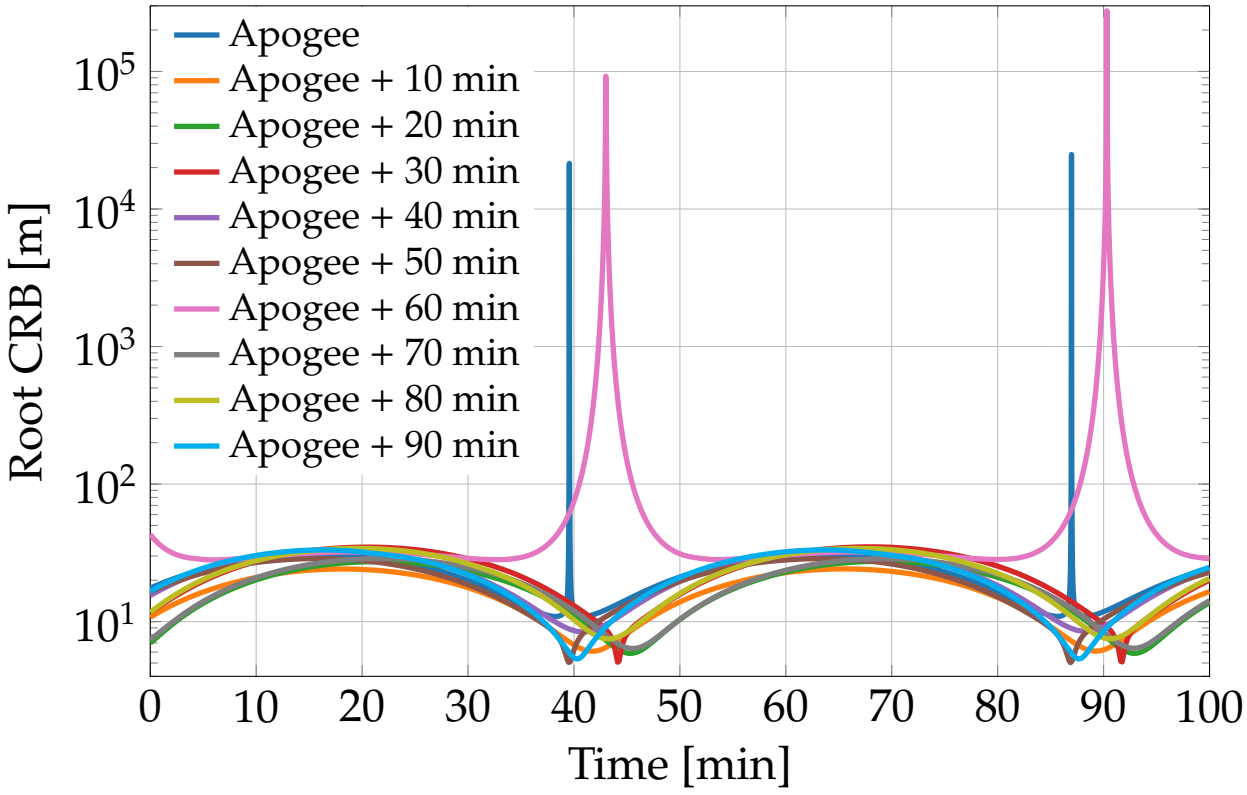

Figure 5.2: Root CRB for deployments towards the positive **y** axis at different points of the orbit. The orbit points are separated by a time-lapse of ten minutes, starting at the apogee.

After selecting the orbit's point for the deployment, I studied the impact of different attitude control and attitude determination systems on the root CRB. Figure 5.3 shows the root CRB of the localization system as both σ_{ADS} and σ_{ACS} increase. The curves are from three days after the deployment to see the effect on the performance. The root CRB is over 100 m for values of σ_{ADS} greater than 0.1°. The difference between having an attitude control system, such as reaction wheels or magnetorquers, with an accuracy of 0.01° or 0.06° is around 20 m in the root CRB value. This information is useful to decide which devices are worth investing in according to the mission.

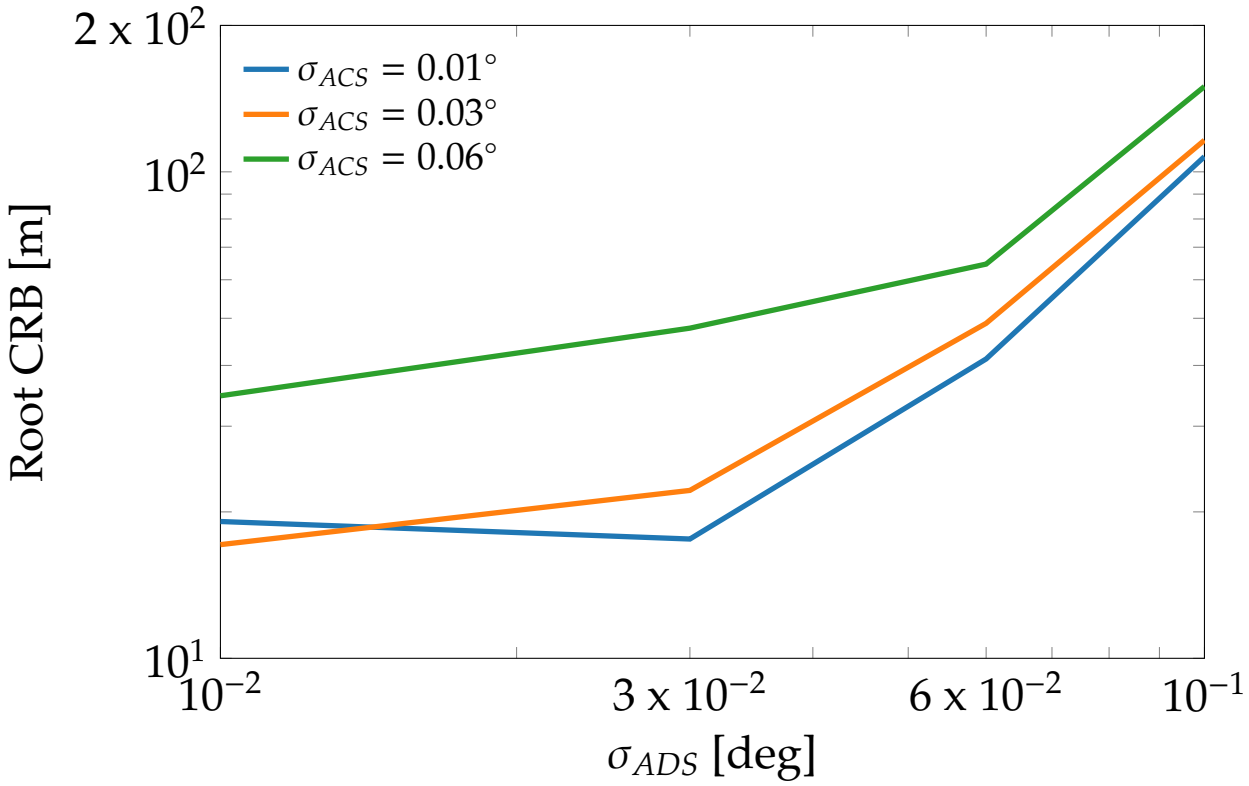

Figure 5.3: Root CRB for different values of σ_{ACS} and σ_{ADS}. These values are related to the accuracy of the deployment system, so I studied the effect on the performance of the localization system three days after deployment.

For the next figures, I display the Root-Mean-Square Error (RMSE) and the estimation bias. The estimation bias shows the distance between the mean estimated position and the real position. The RMSE and the estimated bias are given by Equations (5.2) and (5.3)

$$\text{RMSE}(\mathbf{u}) = \sqrt{\frac{1}{L_0}\sum_{l_0=1}^{L_0}\left(\frac{1}{L}\sum_{l=1}^{L}\|\hat{\mathbf{u}}_l - \mathbf{u}\|^2\right)} \tag{5.2}$$

$$\text{bias}(\mathbf{u}) = \sqrt{\frac{1}{L_0}\sum_{l_0=1}^{L_0}\left\|\frac{1}{L}\left(\sum_{l=1}^{L}\hat{\mathbf{u}}_l\right) - \mathbf{u}\right\|^2}, \tag{5.3}$$

where $\hat{\mathbf{u}}_l$ is the lth ensemble's position estimate, $L = 5,000$ is the number of ensemble runs and $L_0 = 5,000$ is the number of deployment scenarios. In both the RMSE and the estimation bias, I calculate the average of L_0 deployments because I am simulating an ADCS without perfect accuracy. For all the simulations, I set $\sigma_{\text{AOA}} = 1°$ and $\sigma_{\text{RD}} = 10$ m, where σ_{AOA} is the standard deviation of the AOA method, and σ_{RD} is the standard deviation of the TDOA method multiplied by the speed of propagation of the radio waves to transform it into a range difference. I also chose $\sigma_{\text{ADS}} = 0.01°$ which is equal to 36 arcseconds of accuracy and can be obtained with a low-cost star tracker [91]. For the ACS, I used $\sigma_{\text{ACS}} = 0.06°$ because Figure 5.3 shows that below this value, the root CRB decreases by less than 20 m. This value for the ACS is possible for a CubeSat using RWs as seen in [98].

The accuracy of the GNSS devices on board the CubeSats also affects the performance of the localization system. To study the consequences, I simulated 5,000 deployments towards the positive $\mathbf{y}$ axis. Then, I evaluated the localization system three days after deployment. For each deployment, I generated 5,000 zero-mean Gaussian noises with a σ_{GNSS} ranging from 10 m to 120 m. Figure 5.4 shows that the RMSE does not change until the accuracy of the GNSS is 50 m.

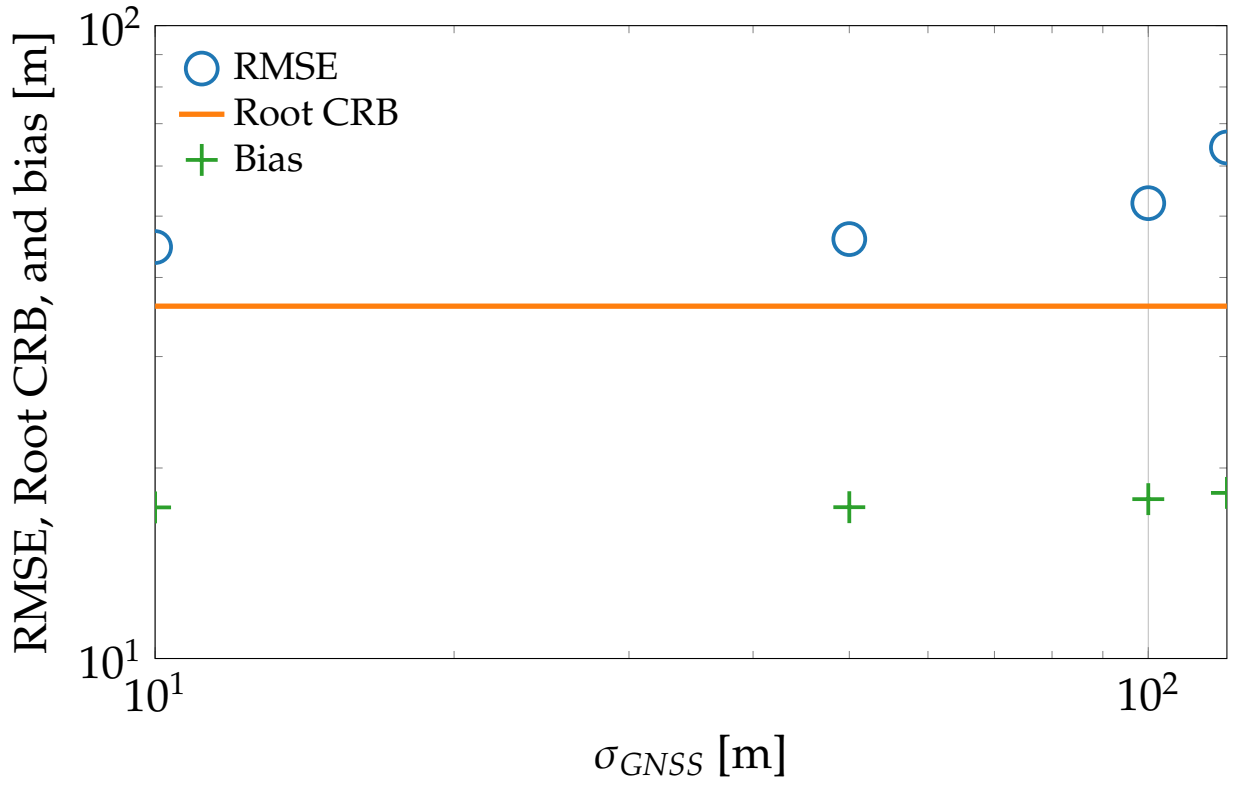

Figure 5.4: Source localization RMSE and bias as σ_{GNSS} increase from 10 m to 120 m three days after the deployment.

For the next simulation, I set $\sigma_{\text{GNSS}} = 10$ m, since there are GNSS devices with that level of accuracy for CubeSats on the market, like the NewSpace Systems (NSS) GPS Receiver from CubeSat Shop. Figure 5.5 shows that the root CRB is below 30 m for most of the orbit three days after deployment. The purple line depicts the distance between

the femto-satellite and the CubeSat that launched it. This distance oscillates and increases over time. This behavior is usual for deployments because, instead of just having a relative speed equal to the deployment speed, what happens is that the orbital parameters change. This change means that the femto-satellite and the CubeSats are now in different orbits. The red line shows the distance between the femto-satellite and the second CubeSat in kilometers. There is no noticeable change in this distance, but this could be related to the scale (kilometers instead of meters like the other curves) and the short time span. These variations may explain the saw-tooth shape of the bias that does not correlate perfectly with the parabolic shape of the angle α nor with the distance between the femto-satellite and the mother-CubeSat.

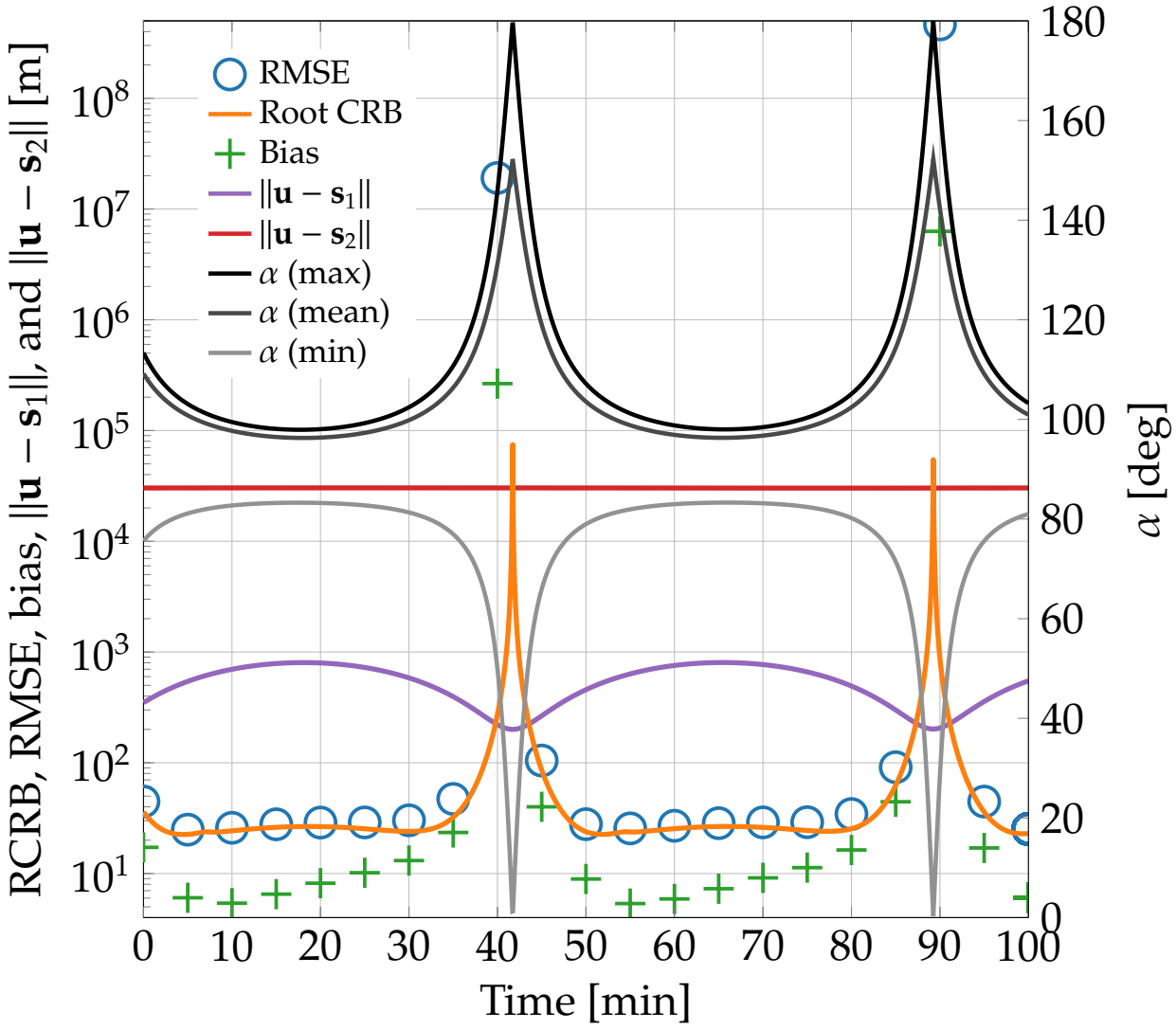

Figure 5.5: Source localization RMSE and bias for the first 100 min after deployment. The line $\|\mathbf{u} - \mathbf{s}_1\|$ is the distance between the femto-satellite and the mother-CubeSat, and the line $\|\mathbf{u} - \mathbf{s}_2\|$ is the distance between the femto-satellite and the second CubeSat. The α line represents the angle between the vector femto-satellite-CubeSat-1 and femto-satellite-CubeSat-2.

I called α the angle formed by the femto-satellite with the two CubeSats. When this angle is near 180°, it means the femto-satellite is between the CubeSats, and when it is near 0°, it means that the mother-CubeSat is between the femto-satellite and the second CubeSat. In the simulations, I calculated the mean of α, the case with the maximum α, and the case with the minimum α. There are cases with angles near 180° or near 0° because the deployment simulation considers the accuracy of the ADCS. Sometimes the femto-satellite is launched towards the positive **y** axis deviated forward, and sometimes, it deviates backward. If we also consider the oscillation of the distance between the femto-satellite and the mother-CubeSat, it is clear why the angle α reaches these values. Figure 5.5 shows that these alignments coincide with the peaks of the root CRB, where the estimation error increases. This increase occurs because these localization geometries are detrimental to the AOA method [99, 100]. I obtained the best results when the angle α is between 80° and 100°.

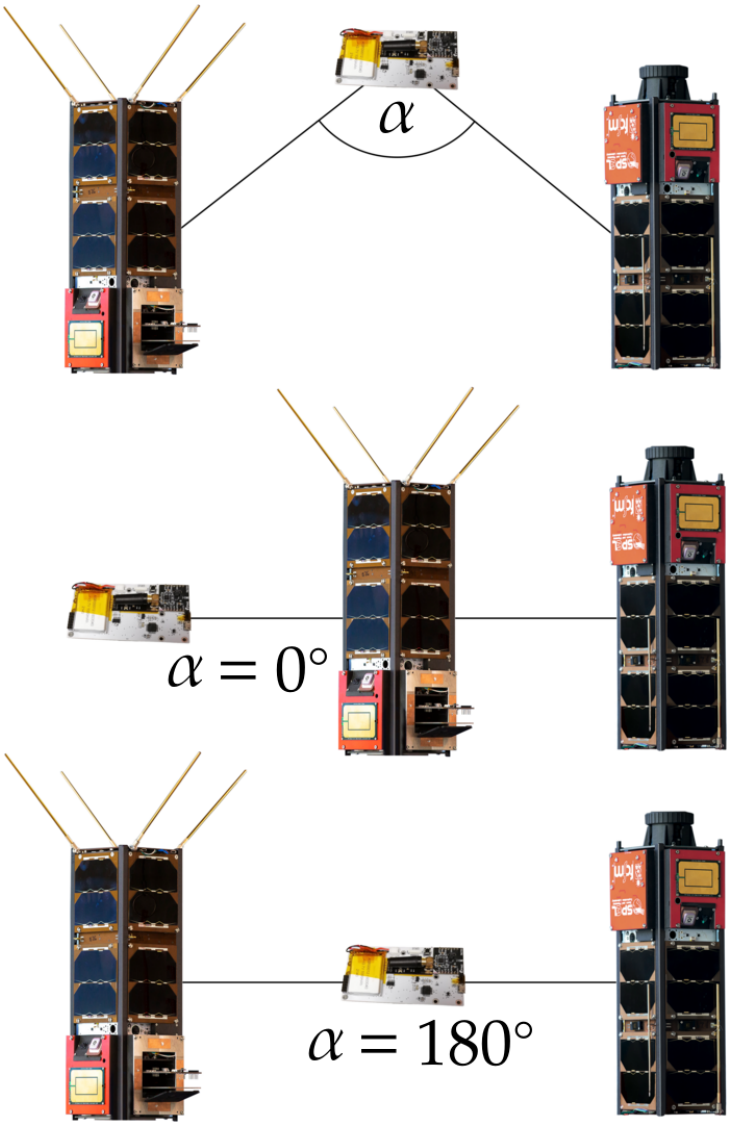

Figure 5.6: α is the angle formed by the three satellites. When α is 0°, it means that one of the CubeSats is between the femto-satellite and the other CubeSat. When α is 180°, it means that the femto-satellite is between the two CubeSats.

5.2 Improving the position estimation

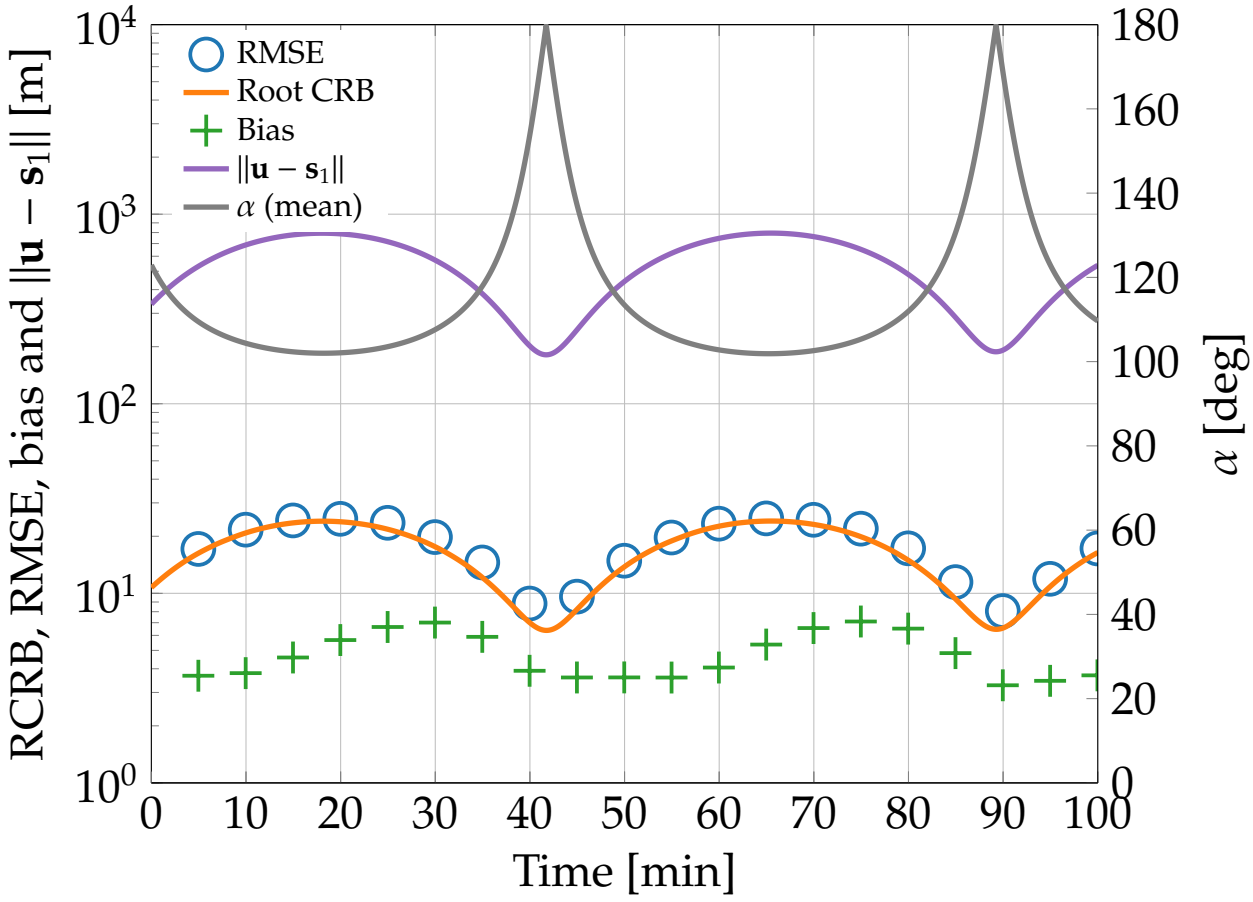

Figure 5.7: This is the deployment scenario that yields the lowest root CRB on average of all the 5,000 deployment simulations. In this scenario, there are no peaks in the root CRB, despite α reaching 180°. The distance between the femto-satellite and the mother-CubeSat is below 1 km.

As I mentioned in the previous section, the alignments between the satellites decrease the performance of the localization system. On the other hand, the satellites are not moving randomly, but they are following an orbit. The orbit of the femto-satellite is *a priori* knowledge that we can use to improve the localization system.

Each deployment simulation produces a different localization geometry. These geometries and localization methods define the root CRB. This bound shows the best position estimation I can achieve in each scenario. In the following simulations, I evaluate different deployment scenarios by themselves, to see if the root CRB has the same pattern with the peaks as the average of the 5,000 deployments. I will also show a method that will allow me to decide whether to trust the estimated position or not.

In the first simulation, I plot the deployment scenario that, due to its geometry, has the lowest root CRB on average of all 5,000 deployment simulations. Figure 5.7 shows that the RMSE of the position estimation is below 30 m in the entire orbit. Let us remember that

these simulations show one orbit three days after the deployment of the femto-satellite from the mother-CubeSat. This figure also shows that despite having an alignment between the satellites, I do not have the uncertainty peaks I showed in the previous plots. This situation will be addressed shortly. For now, let us notice that the angle α is greater than 100°, with a peak at 180°, which means that the femto-satellite is aligned in the middle of the two CubeSats.

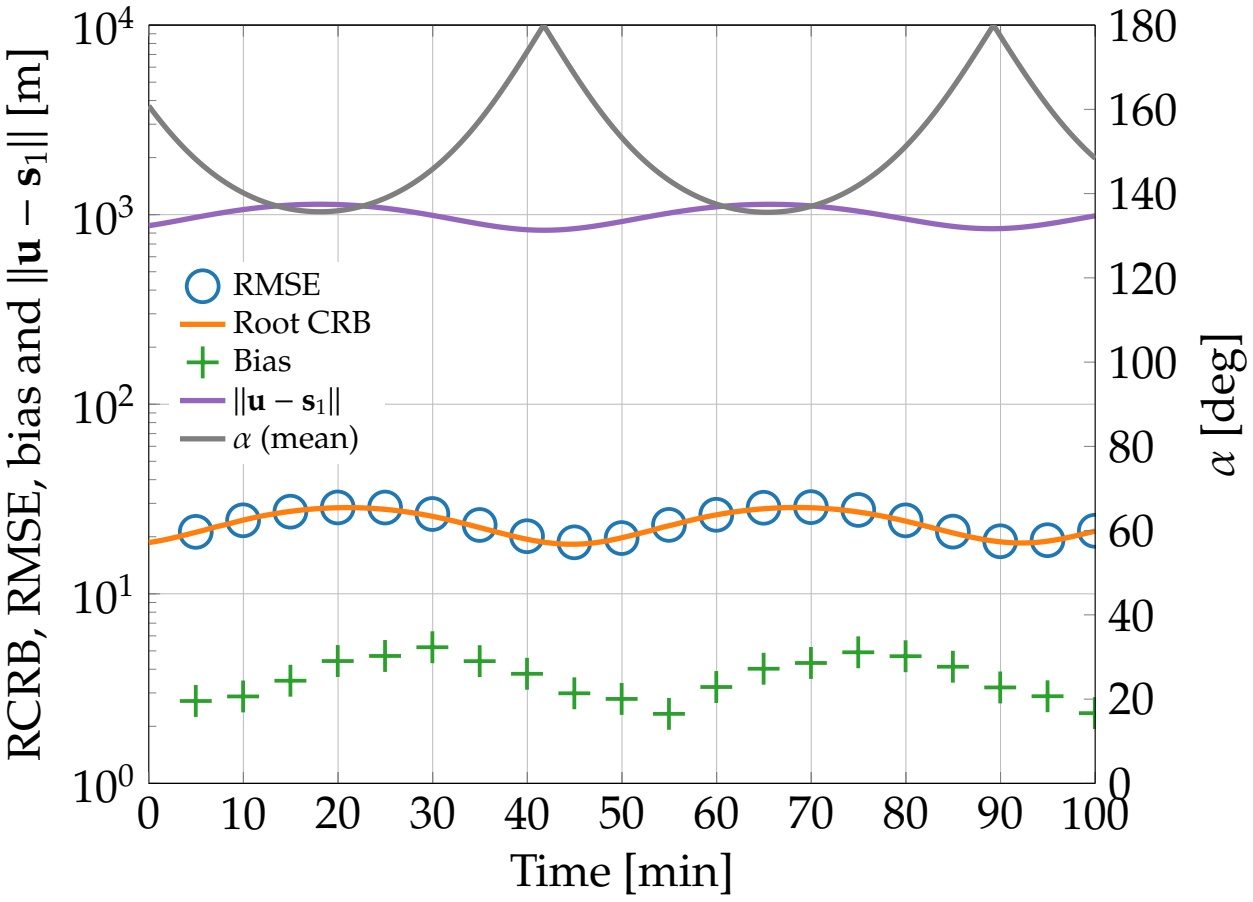

Figure 5.8: This plot shows the scenario with the highest average root CRB of 4,230 simulations.

For the next simulation, I sorted the 5,000 deployment scenarios in terms of the average root CRB. Figure 5.8 shows the scenario with the highest root CRB in 4,230 simulations. In this simulation, the highest RMSE is near 30 m, and the angle α is above 130° however, there are still no peaks in the root CRB. The lowest RMSE is nearly 20 m, and the distance between the femto-satellite and the mother-CubeSat is around 1 km.

Figure 5.9 shows the case with the highest root CRB of all the 5,000 deployment simulations. I had to change the scale due to the peaks of the root CRB, and because of the increase in the estimation bias and in the RMSE. This estimator still could attain the root CRB, except for the vicinity of the peaks, which coincide with the lowest value of the angle α. When this angle is zero, it means that the satellites are aligned, and one of the CubeSats is between the other satellites. The distance between the femto-satellite and the mother-CubeSat is nearly 2 km.

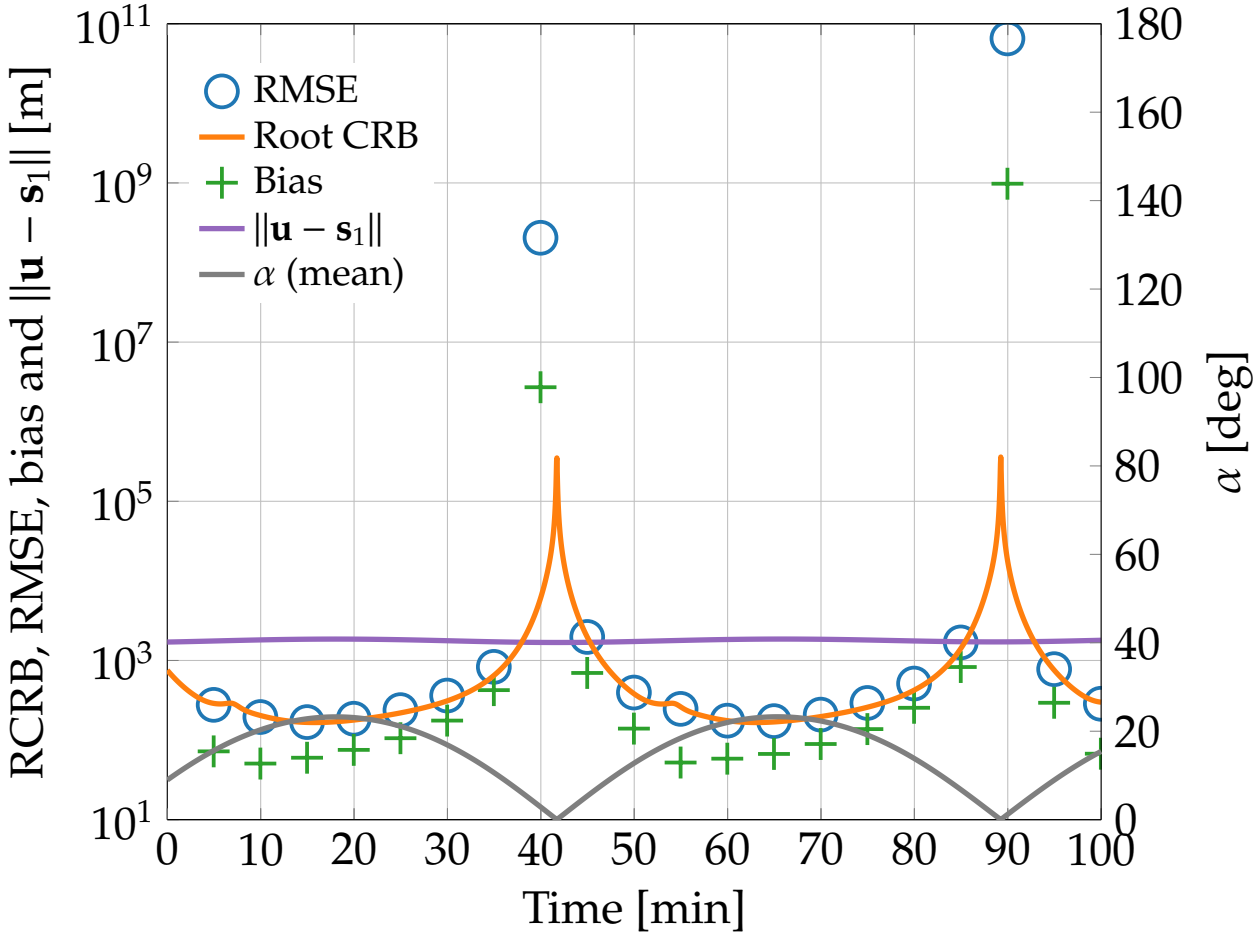

Figure 5.9: This plot shows the scenario with the highest root CRB of 5,000 simulations.

With all this information, it is clear that the first step for improving the position estimation is to develop a method to detect these peaks. For this reason, I run $L = 5,000$ simulations in which I estimated the position using the measurements of TDOA and AOA at one sample per second for 100 minutes. For each simulation, I calculated the distance between the estimated position of the femto-satellite and the position of the mother-CubeSat, including the noise of the CubeSat's GNSS receiver. Figure 5.10 shows the distance of these estimated positions and it is clear that the peaks of this plot are in the same instant as the peaks of the root CRB of the previous figure. After noticing this, I decided to plot the absolute value of the difference between two samples of distance as shown in equation 4.3 and in Figure 5.11. This figure makes these peaks easier to distinguish from the rest of the data, and it is even more clear that those measurements have too much error to be trusted because the distance between these satellites should not change that amount in one second. Therefore, to detect the peaks in the root CRB, I can search for the peaks in the array of these distance differences. The maximum value is one of the peaks, and the other one can be either before or after this peak. To avoid classifying as a peak a point in the vicinity of the maximum value, I established a window around the maximum value so as not to search for the other peak. Then, I find the maximum value previous to this window, and a maximum value after the time window, and compare them. The greater value is the other peak.

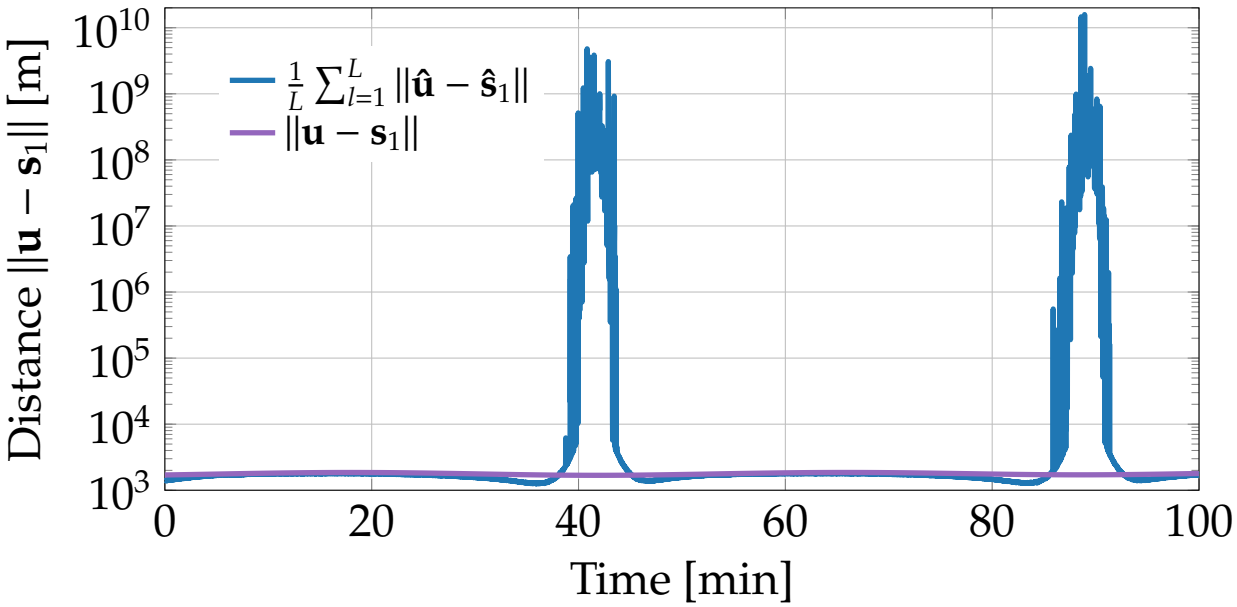

Figure 5.10: This plot shows the scenario with the highest root CRB of the 5,000 deployments. I run 5,000 simulations of this scenario. The blue line is the average distance between the estimated positions between the femto-satellite and the mother-CubeSat. The purple line is the real distance between these satellites. It is clear from this figure that the real distance between these satellites does not change as much as the estimated one for around 20% of the orbit.

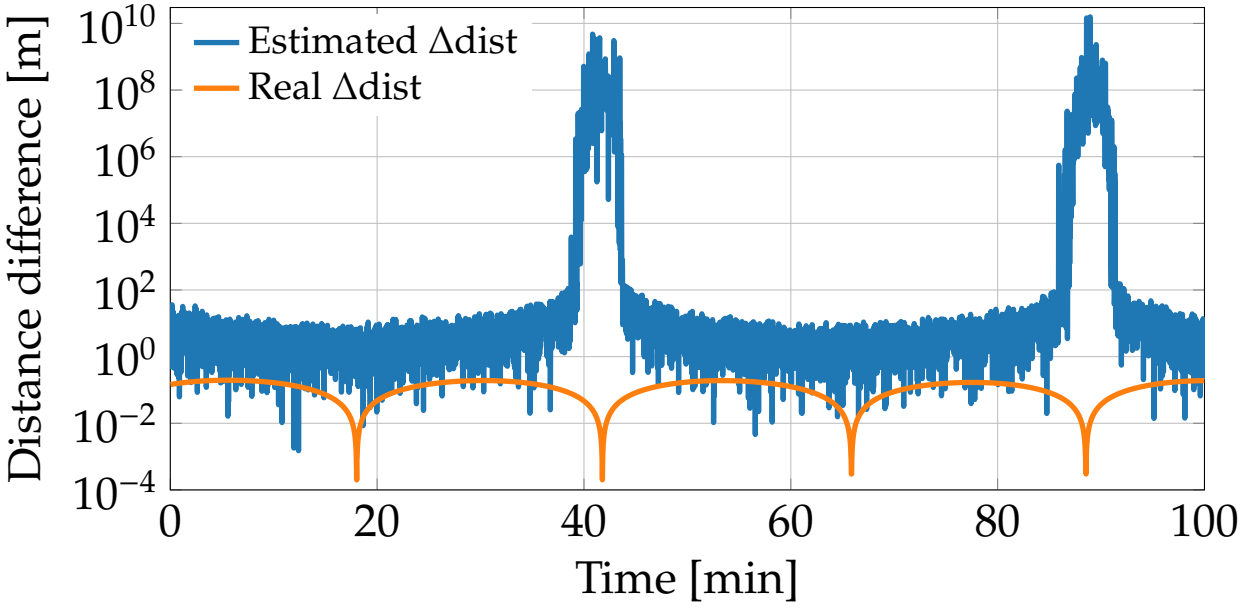

Figure 5.11: This plot shows the scenario with the highest root CRB of the 5,000 deployments. I run 5,000 simulations of this scenario. The blue line is the difference between two consecutive estimated distances of the femto-satellite to the mother-CubeSat. The time intervals with the highest values are in the same instant when the uncertainty of the measurements increases due to the geometry formed by the satellites. This is also the same instant when the root CRB increase for the combination of the AOA with the TDOA method.

After detecting the peaks, I need to establish a time window around the peak where the position estimated with the measurements must be replaced with another method due to the uncertainty of the measurements. To improve the position estimation, I used the HCW dynamic model. After running multiple simulations, I found that I obtain the best results when I use the model seven minutes before the peak, until five minutes after the peak (see eq. 5.4). These intervals are not symmetric due to the increase in the model's accumulated error. Figure 5.12 compares using only the measurements with replacing the measurements with the HCW dynamic model during the time windows where the uncertainty of the measurements is too high.

$$\hat{\boldsymbol{u}}(t) = \begin{cases} (t > t_{peak} + 420) \wedge (t < t_{peak} + 300) & \text{HCW}(t) \\ (t < t_{peak} + 420) \vee (t > t_{peak} + 300) & \text{AOA}(t) + \text{TDOA}(t) \end{cases} \tag{5.4}$$

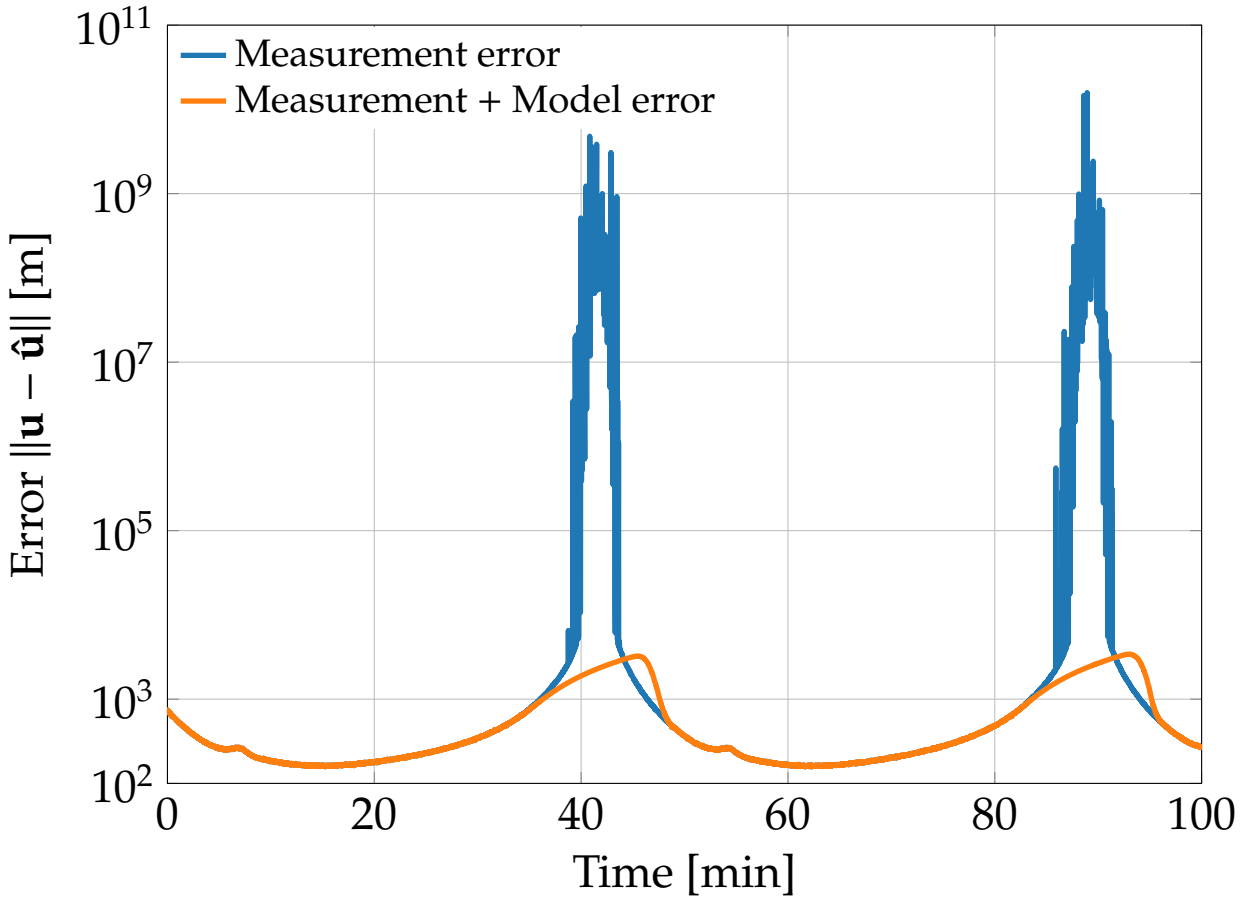

Figure 5.12: This plot shows the scenario with the highest root CRB of the 5,000 deployments. I run 5,000 simulations of this scenario. The blue line is the error using only the measurements, and the orange line is the error of a combination of the measurements with the model. The model reduces the estimation error by more than six orders of magnitude for most of the interval where it is used, at the cost of increasing the error in the last part of the interval.

Figure 5.13 shows the true orbit for this deployment scenario, and the estimated orbit using the measurement and the model. There is no visible difference due to the low error compared to the scale of the plot. This was not the case when using only the measurements.

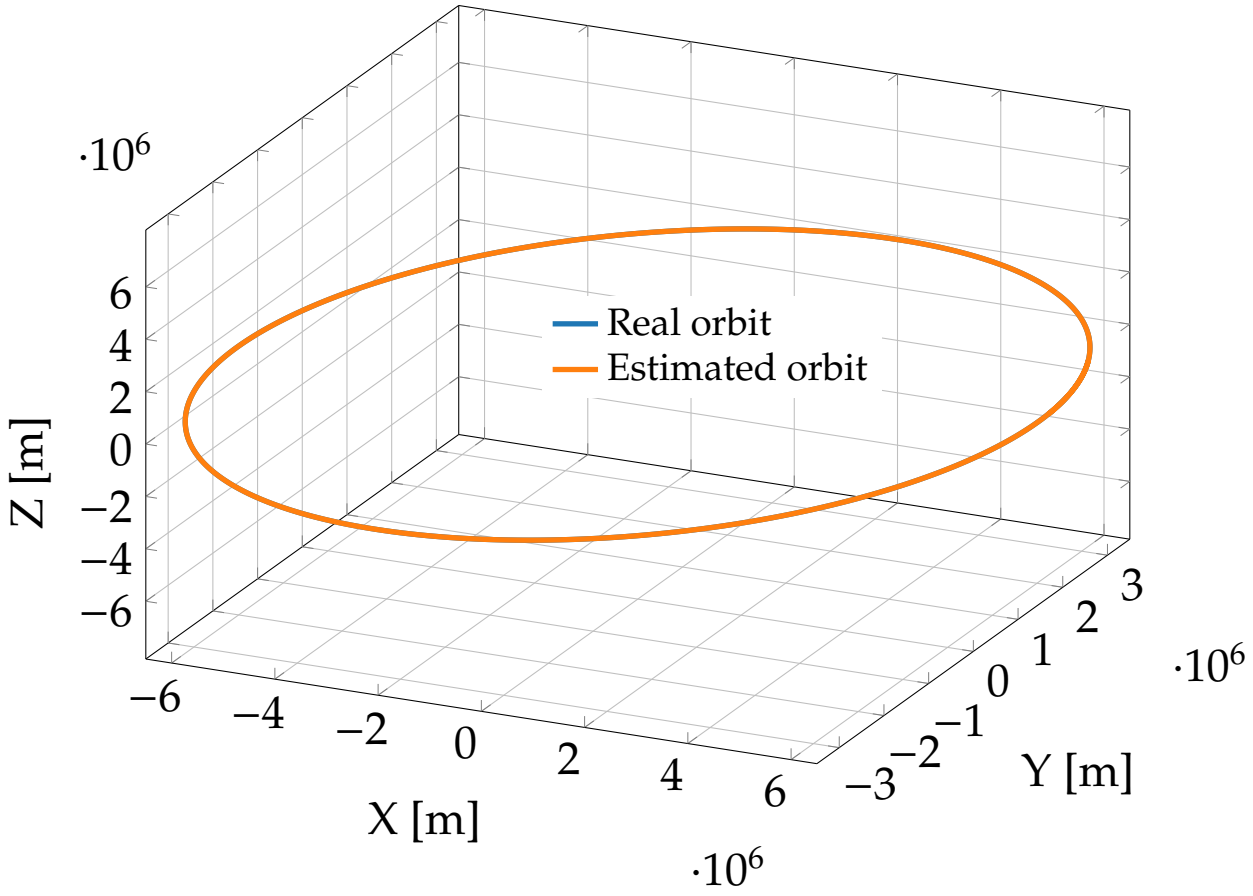

Figure 5.13: This plot shows the scenario with the highest root CRB of the 5,000 deployments. I run 5,000 simulations of this scenario. The blue line is the actual orbit of the femto-satellite. The orange line is the average of the 5,000 estimated orbits using a combination of the model and the measurements. Both orbits are in the ECI coordinate frame.

6. Conclusions

This work presents the adaptation of a method that allows us to geolocalize a source with only two stations in low earth orbit (LEO). I based my work on a methodology intended originally for fix stations located on the ground [33]. My geo-localization method also relies on the radio link between the source and the stations and on a system to combine the time difference of arrival (TDOA) and the angle of arrival (AOA) methods. I evaluated the geo-localization accuracy of this method for several LEO scenarios. The simulated scenarios used two 3U CubeSats (stations) and one femto-satellite (source), which is assumed to be deployed by one of these CubeSats. In contrast to the work by Yin et al. [33], my work allows the sources to go below 0° of elevation of the receiving stations due to the absence of ground and adds the complexity of having moving stations (the two CubeSats). Additionally, I studied the impact that different uncertainties in the location estimation of these CubeSats have on the source location estimation. I simulated the deployment of the femto-satellite from the CubeSat and studied the impact on the source location accuracy for different deployment directions and accuracy levels of the onboard attitude determination and control systems for CubeSats.

I found in my analysis that with the current technology available for CubeSats, there are operational strategies that allow localization of the femto-satellite with an accuracy as good as 30 m, ~80% of the time per orbit. I accomplished this by using only two CubeSats as receiving stations, without the necessity of using GNSS receivers on the source satellite. I will test this in space with the SUCHAI-2 and SUCHAI-3 missions [21] developed by the Space and Planetary Exploration Laboratory (SPEL) at the University of Chile (see Figures 1.1 and 1.2). For the analysis, I developed a simulation tool available on the GitHub of the SPEL (last accessed on February 23rd, 2023): `https://github.com/spel-uchile/Pypredict`.

When one CubeSat is following another one, the simulations show that the performance is highly dependent on the direction of deployment (see Figure 5.1). The best scenario is when I deploy the femto-satellite towards the $\mathbf{y}$ axis, perpendicular to the nadir and the direction of movement of the mother-CubeSat (see the red and green curves in Figure 5.1).

After choosing the direction of deployment, I studied the impact on the accuracy of the source location estimation depending on the point of the orbit where the deployment takes place. I found that these variations were negligible compared to the variations provoked by the deployment direction. Nevertheless, I obtain the lowest root CRB on average when a deployment occurs 10 min after the apogee.

Since the accuracy of the source location estimation is highly dependent on the deployment direction, I analyzed the current attitude and control system technology in their capacity to ensure that the geometry formed by the CubeSats with the femto-satellite is as close to the optimal as possible. By using the reported accuracy of an open-source star tracker [91], I simulated the localization procedure for different accuracies of the attitude determination systems and the attitude control systems, where the lowest simulated values were $\sigma_{ADS} = 0.01°$ and $\sigma_{ACS} = 0.01°$. Figure 5.3 shows that improving the accuracy of the used attitude determination and control systems improves the accuracy of the location estimation. However, the relation is not linear. For instance, the location estimation accuracy obtained with [$\sigma_{ADS} = 0.01°$, $\sigma_{ACS} = 0.01°$] is the same as that reached with [$\sigma_{ADS} = 0.01°$, $\sigma_{ACS} = 0.03°$], and the difference in the location estimation accuracy when using [$\sigma_{ADS} = 0.03°$, $\sigma_{ACS} = 0.03°$] is a few meters less than the accuracy achieved when using [$\sigma_{ADS} = 0.03°$, $\sigma_{ACS} = 0.01°$]. It tells us that for certain attitude control accuracy, there is a point where improving the attitude determination accuracy has a negligible impact on the accuracy of source location estimation.

Then, by using $\sigma_{ADS} = 0.01°$ and $\sigma_{ACS} = 0.06°$, I studied how the accuracy of the onboard GNSS receivers affected the performance of the localization system. The simulations show that when the accuracy of the GNSS receivers is better than 50 m, the RMSE remains more or less constant (see Figure 5.4). Since several GNSS receivers offer $\sigma_{GNSS} = 10$ m of accuracy, I selected this value.

After selecting the deployment direction and the ADCS and GNSS accuracies, I ran a simulation to evaluate the localization accuracy achievable with the TDOA-AOA method. This system achieved a root CRB below 30 m and an RMSE near this value for most of the orbit. The only exception is when the three satellites align with each other, and one of the CubeSats is in between the other satellites. These alignments generate geometries detrimental to the AOA method. Having a third CubeSat not aligned with the rest of the satellites allows the Time Difference Of Arrival (TDOA) method to solve this issue. However, I wanted to know if I could estimate the location using only two CubeSats, not only because the number of stations is lower but also because we have only two CubeSats in our mission [21]. To improve the position estimation in these cases, I made a more in-depth study of the 5,000 deployment scenarios and noticed that 4,230 out of 5,000 of the cases have an RMSE of up to 30 m, using only TDOA with AOA measurements. For the rest of the cases, I proposed a post-processing technique to find the instants when there is an alignment that increases the root CRB. This technique consists of measuring and storing the estimated distance between the femto-satellite and the mother-CubeSat every second for 100 minutes. After this, I searched for the two maximum values of the distance differences, as seen in equation 4.3. These maximum values show when there is an unusual increment of the separation between the femto-satellite and the mother-CubeSat, and it happens at the same moment when the root CRB of the scenario has a peak value. With this information, I use the HCW dynamic model to replace the position estimation of the measurements. I do this for all the estimated positions between seven minutes before a peak to five minutes after the peak. The average of 5,000 simulations of the scenario that yields the highest root CRB shows that this post-process reduces the error by six to seven orders of magnitude, with a maximum position error of around 3.41 km.

These results show the feasibility of performing the remote geo-location of a femto-satellite by using a communication link with patch antenna arrays to estimate the AOA while estimating the TDOA of the signal using a GNSS clock signal. This approach will be tested in space in the SUCHAI-2 and -3 missions. The SUCHAI-3 carries a femto-satellite and will deploy it at the end of its mission. The femto-satellite carries a PNI magnetometer for magnetospheric studies [19, 17], a temperature sensor to calibrate the magnetometer, and an S-band transceiver to communicate with the SUCHAI-2 and SUCHAI-3. The transceiver will also be used to run some tests of the methods proposed in this Thesis. This approach, which includes the method and the deployment strategy, might be relevant for reducing the size, cost, and power consumption of femto-satellites while maintaining accuracy in their location estimation. This method could also be useful for missions at very low altitudes (below 350 km), missions developed for other celestial bodies, and for approaching a satellite to another for docking [78]. In addition, this technique might help estimate the orbits of other satellites in LEO (satellite tracking) by using a small number of CubeSats.

The next task after this work is to deploy the femto-satellite from SUCHAI-3 and to see if we can get some beacons and measure the TDOA and the AOA. The next phase is to find ways to improve the system's accuracy, response time, and reliability. I can test if I can improve the accuracy of the geo-location method using an Unscented Kalman Filter (UKF) to combine the measurements with the HCW model [101, 102]. I need to test this approach and implement it in an embedded system compatible with a CubeSat or a femto-satellite. If it runs successfully during the test on the ground, I can reprogram the CubeSats and test it in orbit or use it in the next mission.

There are ongoing efforts to propose new missions, test new algorithms, and improve the XNAV [103, 104, 105]. There is a proposed CubeSat mission to point a spectrometer to a pulsar for XNAV [106]. If the hardware needed for XNAV is miniaturized, I can test if we can estimate the position of a CubeSat using this technology. The next step will be to use two CubeSats with this navigation technique to estimate a femto-satellite position using the method simulated in this Thesis. With this system, the CubeSats will not need a GNSS constellation to know their location. They will be able to go to deep-space missions and estimate the position of their femto-satellites using my method.

Bibliography

[1] D. Munoz, F. B. Lara, C. Vargas, and R. Enriquez-Caldera, *Position location techniques and applications*. Academic Press, 2009.

[2] H. D. Curtis, *Orbital mechanics for engineering students*. Butterworth-Heinemann is an imprint of Elsevier, 2014.

[3] S. Tomic, M. Beko, and R. Dinis, "3-D Target Localization in Wireless Sensor Networks Using RSS and AoA Measurements," *IEEE Transactions on Vehicular Technology*, vol. 66, no. 4, p. 3197–3210, 2017.

[4] Y. Chan, F. Chan, W. Read, B. Jackson, and B. Lee, "Hybrid localization of an emitter by combining angle-of-arrival and received signal strength measurements," *2014 IEEE 27th Canadian Conference on Electrical and Computer Engineering (CCECE)*, 2014.

[5] H. Qi, L. Mo, and X. Wu, "SDP Relaxation Methods for RSS/AOA-Based Localization in Sensor Networks," *IEEE Access*, vol. 8, p. 55113–55124, 2020.

[6] J. Chen and A. Abedi, "A Hybrid Framework for Radio Localization in Broadband Wireless Systems," *2010 IEEE Global Telecommunications Conference GLOBECOM 2010*, 2010.

[7] A. Tahat, G. Kaddoum, S. Yousefi, S. Valaee, and F. Gagnon, "A Look at the Recent Wireless Positioning Techniques with a Focus on Algorithms for Moving Receivers," *IEEE Access*, vol. 4, p. 6652–6680, 2016.

[8] Y.-Y. Li, G.-Q. Qi, and A.-D. Sheng, "Performance Metric on the Best Achievable Accuracy for Hybrid TOA/AOA Target Localization," *IEEE Communications Letters*, vol. 22, no. 7, p. 1474–1477, 2018.

[9] Y. Chan and K. Ho, "A simple and efficient estimator for hyperbolic location," *IEEE Transactions on Signal Processing*, vol. 42, no. 8, p. 1905–1915, 1994.

[10] Y. Zhao, Z. Li, B. Hao, J. Si, and P. Wan, "Bias reduced method for TDOA and AOA localization in the presence of sensor errors," *2017 IEEE International Conference on Communications (ICC)*, 2017.

[11] X. Jin-Yu, W. Wei, and Z. Zhong-Liang, "A new TDOA location technique based on

Taylor series expansion in cellular networks," *Proceedings of the 8th International Scientific and Practical Conference of Students, Post-graduates and Young Scientists. Modern Technique and Technologies. MTT2002 (Cat. No.02EX550)*, 2003.

[12] B. Jin, X. Xu, and T. Zhang, "Robust Time-Difference-of-Arrival (TDOA) Localization Using Weighted Least Squares with Cone Tangent Plane Constraint," *Sensors*, vol. 18, p. 778, Apr 2018.

[13] A. Belli and P. Exertier, "Long-term behavior of the doris oscillator under radiation: The jason-2 case," *IEEE transactions on ultrasonics, ferroelectrics, and frequency control*, vol. 65, no. 10, pp. 1965–1976, 2018.

[14] Z. Manchester, M. Peck, and A. Filo, "Kicksat: A crowd-funded mission to demonstrate the world's smallest spacecraft," *Proc. Small Satellite Conf.*, 2013.

[15] F. Y. Hadaegh, S.-J. Chung, and H. M. Manohara, "On Development of 100-Gram-Class Spacecraft for Swarm Applications," *IEEE Systems Journal*, vol. 10, no. 2, p. 673–684, 2016.

[16] D. Barnhart, T. Vladimirova, M. Sweeting, R. Balthazor, L. Enloe, H. Krause, T. Lawrence, M. McHarg, J. Lyke, J. White, *et al.*, "Enabling space sensor networks with pcbsat," *Proc. Small Satellite Conference*, 2007.

[17] J. B. Parham, M. Kromis, D. Einhorn, P. Teng, S. Posnov, H. Levin, O. Van Dessel, A. Zosuls, B. Walsh, and J. Semeter, "Networked small satellite magnetometers for auroral plasma science," *Journal of Small Satellites*, vol. 8, no. 1, pp. 801–814, 2019.

[18] L. Yang, J. Guo, C. Fan, X. Song, S. Wu, and Y. Zhao, "The design and experiment of stardust femto-satellite," *Acta Astronautica*, vol. 174, pp. 72–81, 2020.

[19] L. H. Regoli, M. B. Moldwin, M. Pellioni, B. Bronner, K. Hite, A. Sheinker, and B. M. Ponder, "Investigation of a low-cost magneto-inductive magnetometer for space science applications," *Geoscientific Instrumentation, Methods and Data Systems*, vol. 7, no. 1, pp. 129–142, 2018.

[20] T. R. Perez and K. Subbarao, "A Survey of Current Femto-Satellite Designs, Technologies, and Mission Concepts," *Journal of Small Satellites*, vol. 5, no. 3), pp. 467–482, 2016.

[21] M. Diaz, J. Zagal, C. Falcon, M. Stepanova, J. Valdivia, M. Martinez-Ledesma, J. Diaz-Pena, F. Jaramillo, N. Romanova, E. Pacheco, *et al.*, "New opportunities offered by Cubesats for space research in Latin America: The SUCHAI project case," *Advances in Space Research*, vol. 58, no. 10, pp. 2134–2147, 2016.

[22] C. Gonzalez, C. Rojas, A. Becerra, J. Rojas, T. Opazo, and M. Diaz, "Lessons learned from building the first chilean nano-satellite: The suchai project," *Proceedings of the Small Satellite Conference*, 2018.

[23] C. Haines, M. Owens, L. Barnard, M. Lockwood, and A. Ruffenach, "The variation of

geomagnetic storm duration with intensity," *Solar Physics*, vol. 294, no. 11, pp. 1–15, 2019.

[24] D. Mototolea and C. Stolk, "Detection and localization of small drones using commercial off-the-shelf fpga based software defined radio systems," in *2018 International Conference on Communications (COMM)*, pp. 465–470, IEEE, 2018.

[25] R. Yamasaki, A. Ogino, T. Tamaki, T. Uta, N. Matsuzawa, and T. Kato, "TDOA location system for IEEE 802.11 b WLAN," in *IEEE Wireless Communications and Networking Conference, 2005*, vol. 4, pp. 2338–2343, IEEE, 2005.

[26] J. Chen, T. Shi, Y. Liu, and S. Wu, "A Time-compensation TDOA-based Wireless Positioning Method for Multi-level IoT Positioning," in *2019 15th International Wireless Communications & Mobile Computing Conference (IWCMC)*, pp. 1731–1736, IEEE, 2019.

[27] W. Li, Q. Tang, C. Huang, C. Ren, and Y. Li, "A new close form location algorithm with AOA and TDOA for mobile user," *Wireless Personal Communications*, vol. 97, no. 2, pp. 3061–3080, 2017.

[28] M. Kaliuzhnyi, F. Bushuev, O. Shulga, Y. Sybiryakova, L. Shakun, V. Bezrukovs, S. Moskalenko, V. Kulishenko, and Y. Malynovskyi, "International network of passive correlation ranging for orbit determination of a geostationary satellite," *Odessa Astronomical Publications*, vol. 29, pp. 203–206, 2016.

[29] S. Shuster, A. J. Sinclair, and T. A. Lovell, "Initial relative-orbit determination using heterogeneous TDOA," in *2017 IEEE Aerospace Conference*, pp. 1–7, IEEE, 2017.

[30] P. Kułakowski, J. Vales-Alonso, E. Egea-López, W. Ludwin, and J. García-Haro, "Angle-of-arrival localization based on antenna arrays for wireless sensor networks," *Computers & Electrical Engineering*, vol. 36, no. 6, pp. 1181–1186, 2010.

[31] E. Y. Menta, N. Malm, R. Jäntti, K. Ruttik, M. Costa, and K. Leppänen, "On the performance of aoa–based localization in 5g ultra–dense networks," *IEEE Access*, vol. 7, pp. 33870–33880, 2019.

[32] Y. Z. Bin, W. Lei, C. P. Qun, and L. A. Nan, "Passive satellite localization using TDOA/FDOA/AOA measurements," *IEEE Conference Anthology*, 2013.

[33] J. Yin, Q. Wan, S. Yang, and K. Ho, "A simple and accurate TDOA-AOA localization method using two stations," *IEEE Signal Processing Letters*, vol. 23, no. 1, pp. 144–148, 2015.

[34] D. Vallado, P. Crawford, R. Hujsak, and T. Kelso, "Revisiting spacetrack report# 3," in *AIAA/AAS Astrodynamics Specialist Conference and Exhibit*, p. 6753, 2006.

[35] M. G. Vidal-Valladares and M. A. Díaz, "A femto-satellite localization method based on tdoa and aoa using two cubesats," *Remote Sensing*, vol. 14, no. 5, p. 1101, 2022.

[36] W. H. Guier and G. C. Weiffenbach, "Theoretical analysis of doppler radio signals

from earth satellites," *Nature*, vol. 181, pp. 1525–1526, 1958.

[37] W. H. Guier and G. C. Weiffenbach, "The doppler determination of orbits," tech. rep., JOHNS HOPKINS UNIV LAUREL MD APPLIED PHYSICS LAB, 1959.

[38] J. Buisson and T. McCaskill, "Timation navigation satellite system constellation study," tech. rep., NAVAL RESEARCH LAB WASHINGTON DC, 1972.

[39] B. Parkinson, "Navstar: Global positioning system an evolutionary research and development program," in *NASA. Goddard Space Flight Center Proc. of the Sixth Ann. Precise Time and Time Interval (PTTI) Planning Meeting*, 1974.

[40] S. A. Nichols, J. D. White, and F. Danzy, "Design and ground test of the nts-1 frequency standard system," *Naval Research Lab. Report*, 1975.

[41] I. Kawano, M. Mokuno, S. Kogure, and M. Kishimoto, "Japanese experimental gps augmentation using quasi-zenith satellite system (qzss)," in *Proceedings of the 17th International Technical Meeting of the Satellite Division of The Institute of Navigation (ION GNSS 2004)*, pp. 175–181, 2004.

[42] V. G. Rao, G. Lachapelle, and S. VijayKumar, "Analysis of irnss over indian subcontinent," in *Proceedings of the 2011 international technical meeting of the institute of navigation*, pp. 1150–1162, 2011.

[43] U.S. Coast Guard Navigation Center, "GPS Constellation." `https://navcen.uscg.gov/gps-constellation`, 2023. Accessed: 2023-02-09.

[44] G. Directorate, "Navstar gps space segment navigation user segment interfaces, interface specification (is-gps-200)," *Global Positioning System Directorate, Revision N*, 2022.

[45] K. Krasuski and S. Savchuk, "Accuracy assessment of aircraft positioning using the dual-frequency gps code observations in aviation," *Communications-Scientific letters of the University of Zilina*, vol. 22, no. 2, pp. 23–30, 2020.

[46] S. Zaminpardaz, P. J. Teunissen, and A. Khodabandeh, "Glonass–only fdma+ cdma rtk: performance and outlook," *GPS Solutions*, vol. 25, no. 3, p. 96, 2021.

[47] Z.-P. Zhang, H.-F. Zhang, W.-Z. Chen, P. Li, W.-D. Meng, Y.-M. Wang, J. Wang, W. Hu, and F.-M. Yang, "Design and performances of laser retro-reflector arrays for beidou navigation satellites and slr observations," *Advances in Space Research*, vol. 54, no. 5, pp. 811–817, 2014.

[48] G. Bury, K. Sośnica, and R. Zajdel, "Multi-gnss orbit determination using satellite laser ranging," *Journal of Geodesy*, vol. 93, no. 12, pp. 2447–2463, 2019.

[49] European Union, "OS SIS ICD: Open Service Signal In Space Interface Control Document, Issue 2.0." `https://www.gsc-europa.eu/sites/default/files/sites/all/files/Galileo_OS_SIS_ICD_v2.0.pdf`, 2021. Accessed: 2023-02-10.

[50] J. F. San-Juan, I. Pérez, M. San-Martín, and E. P. Vergara, "Hybrid SGP4 orbit propagator," *Acta Astronautica*, vol. 137, p. 254–260, 2017.

[51] C. Ardito, J. Morales, J. Khalife, A. Abdallah, and Z. Kassas, "Performance evaluation of navigation using LEO satellite signals with periodically transmitted satellite positions," in *Proceedings of ION International Technical Meeting Conference*, pp. 306–318, 2019.

[52] H. Peng and X. Bai, "Gaussian Processes for improving orbit prediction accuracy," *Acta Astronautica*, vol. 161, p. 44–56, 2019.

[53] X. Liu, B. Yuan, and Z. Meng, "Microsatellite Autonomous Orbit Propagation Method Based on SGP4 Model and GPS Data," *2018 IEEE CSAA Guidance, Navigation and Control Conference (CGNCC)*, 2018.

[54] S. T. Goh and K.-S. Low, "Real-time estimation of satellites two-line elements via positioning data," *2018 IEEE Aerospace Conference*, 2018.

[55] M. Alawieh, N. Hadaschik, N. Franke, and C. Mutschler, "Inter-satellite ranging in the Low Earth Orbit," *2016 10th International Symposium on Communication Systems, Networks and Digital Signal Processing (CSNDSP)*, 2016.

[56] Z. Bouhanna and C. Bridges, "Relative range estimation using SDR for space traffic management," in *2018 IEEE Aerospace Conference*, pp. 1–9, IEEE, 2018.

[57] N. E. Gemayel, S. Koslowski, F. K. Jondral, and J. Tschan, "A low cost TDOA localization system: Setup, challenges and results," *2013 10th Workshop on Positioning, Navigation and Communication (WPNC)*, 2013.

[58] Z. Li, D. C. Dimitrova, T. Braun, and D. Rosário, "Highly accurate evaluation of gps synchronization for tdoa localization," in *2013 IFIP Wireless Days (WD)*, pp. 1–3, IEEE, 2013.

[59] S. Xu and K. Doğançay, "Optimal sensor placement for 3-d angle-of-arrival target localization," *IEEE Transactions on Aerospace and Electronic Systems*, vol. 53, no. 3, pp. 1196–1211, 2017.

[60] C.-D. Wann, Y.-J. Yeh, and C.-S. Hsueh, "Hybrid tdoa/aoa indoor positioning and tracking using extended kalman filters," in *2006 IEEE 63rd Vehicular Technology Conference*, vol. 3, pp. 1058–1062, IEEE, 2006.

[61] X. Li, Y. Xing, and Z. Zhang, "A hybrid aoa and tdoa-based localization method using only two stations," *International Journal of Antennas and Propagation*, vol. 2021, 2021.

[62] T. M. Hackett, M. Johnston, and S. G. Bilen, "Spacecraft block scheduling for nasa's deep space network," in *2018 SpaceOps Conference*, p. 2578, 2018.

[63] A. Hewish, P. Scott, and D. Wills, "Interplanetary scintillation of small diameter

radio sources," *Nature*, vol. 203, pp. 1214–1217, 1964.

[64] A. Hewish, "Pulsars," *Scientific American*, vol. 219, no. 4, pp. 25–35, 1968.

[65] G. Downs, "Interplanetary navigation using pulsating radio sources," tech. rep., Jet Propulsion Laboratory, California Institute of Technology, 1974.

[66] J. Taylor, "Millisecond pulsars: Nature's most stable clocks," *Proceedings of the IEEE*, vol. 79, no. 7, pp. 1054–1062, 1991.

[67] R. N. Manchester, G. B. Hobbs, A. Teoh, and M. Hobbs, "The australia telescope national facility pulsar catalogue," *The Astronomical Journal*, vol. 129, no. 4, p. 1993, 2005.

[68] X. Zhang, P. Shuai, L. Huang, S. Chen, and L. Xu, "Mission overview and initial observation results of the x-ray pulsar navigation-i satellite," *International Journal of Aerospace Engineering*, vol. 2017, 2017.

[69] J. W. Mitchell, M. Hassouneh, L. Winternitz, J. Valdez, S. Price, S. R. Semper, W. H. Yu, Z. Arzoumanian, P. Ray, K. S. Wood, *et al.*, "Sextant-station explorer for x-ray timing and navigation technology," in *AIAA Guidance, Navigation, and Control Conference*, p. 0865, 2015.

[70] L. M. Winternitz, J. W. Mitchell, M. A. Hassouneh, J. E. Valdez, S. R. Price, S. R. Semper, H. Y. Wayne, P. S. Ray, K. S. Wood, Z. Arzoumanian, *et al.*, "Sextant x-ray pulsar navigation demonstration: Flight system and test results," in *2016 IEEE Aerospace Conference*, pp. 1–11, IEEE, 2016.

[71] J. W. Mitchell, L. M. Winternitz, M. A. Hassouneh, S. R. Price, S. R. Semper, W. H. Yu, P. S. Ray, M. T. Wolff, M. Kerr, K. S. Wood, *et al.*, "Sextant x-ray pulsar navigation demonstration: Initial on-orbit results," in *Annual American Astronautical Society (AAS) Guidance and Control Conference 2018*, 2018.

[72] L. B. Winternitz, M. A. Hassouneh, J. W. Mitchell, S. R. Price, W. H. Yu, S. R. Semper, P. S. Ray, K. S. Wood, Z. Arzoumanian, and K. C. Gendreau, "Sextant x-ray pulsar navigation demonstration: Additional on-orbit results," in *2018 SpaceOps Conference*, p. 2538, 2018.

[73] S. Zheng, S. Zhang, F. Lu, W. Wang, Y. Gao, T. Li, L. Song, M. Ge, D. Han, Y. Chen, *et al.*, "In-orbit demonstration of x-ray pulsar navigation with the insight-hxmt satellite," *The Astrophysical Journal Supplement Series*, vol. 244, no. 1, p. 1, 2019.

[74] R. Raymond Karimi and D. Mortari, "Interplanetary autonomous navigation using visible planets," *Journal of Guidance, Control, and Dynamics*, vol. 38, no. 6, pp. 1151–1156, 2015.

[75] D. Mortari and D. Conway, "Single-point position estimation in interplanetary trajectories using star trackers," *Celestial Mechanics and Dynamical Astronomy*, vol. 128, pp. 115–130, 2017.

[76] E. Andreis, V. Franzese, F. Topputo, *et al.*, "An overview of autonomous optical navigation for deep-space cubesats," in *International Astronautical Congress: IAC Proceedings*, pp. 1–11, 2021.

[77] E. Andreis, P. Panicucci, V. Franzese, F. Topputo, *et al.*, "A vision-based navigation algorithm for autonomous deep-space cruise," in *3rd Space Imaging Workshop*, pp. 1–10, 2022.

[78] M. Ikura, S. Ikari, A. Tomiki, R. Funase, and S. Nakasuka, "Estimation Algorithm of Relative Position and Attitude during Proximity Rendezvous Using Multiple Ultra-Wide-Band Devices," *Transactions of the Japan Society for Aeronautical and Space Sciences, Aerospace Technology Japan*, vol. 17, no. 1, pp. 43–50, 2019.

[79] S. Battistini, G. De Angelis, M. Pontani, and F. Graziani, "An iterative guidance and navigation algorithm for orbit rendezvous of cooperating cubesats," *Applied Sciences*, vol. 12, no. 18, p. 9250, 2022.

[80] F. Ferrari, V. Franzese, M. Pugliatti, C. Giordano, and F. Topputo, "Preliminary mission profile of hera's milani cubesat," *Advances in Space Research*, vol. 67, no. 6, pp. 2010–2029, 2021.

[81] F. W. Alsaade, Q. Yao, M. S. Al-Zahrani, A. S. Alzahrani, and H. Jahanshahi, "Indirect-neural-approximation-based fault-tolerant integrated attitude and position control of spacecraft proximity operations," *Sensors*, vol. 22, no. 5, p. 1726, 2022.

[82] J. Bowen, M. Villa, and A. Williams, "Cubesat based rendezvous, proximity operations, and docking in the cpod mission," *Proceedings of the 29th Annual AIAA/USU Conference on Small Satellites*, 2015.

[83] F. Branz, L. Olivieri, F. Sansone, and A. Francesconi, "Miniature docking mechanism for cubesats," *Acta Astronautica*, vol. 176, pp. 510–519, 2020.

[84] S. Kang, Y. Song, and S.-Y. Park, "Nanosat formation flying design for snipe mission," *Journal of Astronomy and Space Sciences*, vol. 37, no. 1, pp. 51–60, 2020.

[85] S. Ikari, H. Kondo, and S. Nakasuka, "Seirios: A demonstration of space infrared interferometer by formation flying of micro-satellites," *Proceedings of the Mission Operations & Autonomy Small Satellite Conference*, 2021.

[86] Z. Guang, B. Xingzi, and L. Bin, "Optimal deployment of spin-stabilized tethered formations with continuous thrusters," *Nonlinear Dynamics*, vol. 95, pp. 2143–2162, 2019.

[87] J. S. Umansky-Castro, K. G. Yap, and M. A. Peck, "Chipsats for planetary exploration: Dynamics and aerothermal modeling of atmospheric entry and dispersion," *Frontiers in Astronomy and Space Sciences*, vol. 8, p. 664215, 2021.

[88] Y. Miyazaki, "Deployable techniques for small satellites," *Proceedings of the IEEE*, vol. 106, no. 3, pp. 471–483, 2018.

[89] L. Lim, T. Bui, Z. Lau, J. Soon, J. Lew, H. Aung, C. Ye, K. Low, S. Goh, S. Chen, *et al.*, "Development and design challenges in VELOX-I nanosatellite," in *2015 International Conference on Space Science and Communication (IconSpace)*, pp. 158–163, IEEE, 2015.

[90] A. P. Kailaje, P. Tapadia, H. Ganti, M. Brindavan, A. Paliva, V. Thakurta, and A. A. Kumar, "Implementation of Wire Burn Deployment Mechanism Using COTS Resistors and Related Investigations," in *2019 IEEE Aerospace Conference*, pp. 1–9, IEEE, 2019.

[91] S. T. Gutiérrez, C. I. Fuentes, and M. A. Díaz, "Introducing sost: An ultra-low-cost star tracker concept based on a raspberry pi and open-source astronomy software," *IEEE Access*, vol. 8, pp. 166320–166334, 2020.

[92] W. Clohessy and R. Wiltshire, "Terminal guidance system for satellite rendezvous," *Journal of the Aerospace Sciences*, vol. 27, no. 9, pp. 653–658, 1960.

[93] E. A. Butcher, J. Wang, and T. A. Lovell, "On kalman filtering and observability in nonlinear sequential relative orbit estimation," *Journal of Guidance, Control, and Dynamics*, vol. 40, no. 9, pp. 2167–2182, 2017.

[94] B. Hofmann-Wellenhof, H. Lichtenegger, and E. Wasle, *GNSS–global navigation satellite systems: GPS, GLONASS, Galileo, and more*. Springer Science & Business Media, 2007.

[95] G. Díaz, "Desarrollo de un sistema de control de orientación usando ruedas de reacción de bajo costo para nano-satélite Suchai.," bachelor's thesis, University of Chile, 2018.

[96] C. E. Gonzalez, C. J. Rojas, A. Bergel, and M. A. Diaz, "An architecture-tracking approach to evaluate a modular and extensible flight software for cubesat nanosatellites," *IEEE Access*, vol. 7, pp. 126409–126429, 2019.

[97] T. Gutierrez, A. Bergel, C. E. Gonzalez, C. J. Rojas, and M. A. Diaz, "Systematic fuzz testing techniques on a nanosatellite flight software for agile mission development," *IEEE Access*, vol. 9, pp. 114008–114021, 2021.

[98] J. Shields, C. Pong, K. Lo, L. Jones, S. Mohan, C. Marom, I. McKinley, W. Wilson, and L. Andrade, "Characterization of cubesat reaction wheel assemblies," *Journal of Small Satellites*, vol. 6, no. 1, pp. 565–580, 2017.

[99] K. Doğançay and H. Hmam, "Optimal angular sensor separation for aoa localization," *Signal Processing*, vol. 88, no. 5, pp. 1248–1260, 2008.

[100] A. N. Bishop, B. Fidan, K. Doğançay, B. D. Anderson, and P. N. Pathirana, "Exploiting geometry for improved hybrid aoa/tdoa-based localization," *Signal Processing*, vol. 88, no. 7, pp. 1775–1791, 2008.

[101] S. K. Biswas and E. Cetin, "Gnss interference source tracking using kalman filters," in *2020 IEEE/ION Position, Location and Navigation Symposium (PLANS)*, pp. 877–882,

2020.

[102] G. Y. Kulikov and M. Kulikova, "Nirk-based cholesky-factorized square-root accurate continuous-discrete unscented kalman filters for state estimation in nonlinear continuous-time stochastic models with discrete measurements," *Applied Numerical Mathematics*, vol. 147, pp. 196–221, 2020.

[103] J. Liu, W. Wang, H. Zhang, L. Shu, and Y. Gao, "Autonomous orbit determination and timekeeping in lunar distant retrograde orbits by observing x-ray pulsars," *Navigation*, vol. 68, no. 4, pp. 687–708, 2021.

[104] Y. Wang, S. Zhang, M. Ge, W. Zheng, X. Chen, S. Zheng, and F. Lu, "Fast on-orbit pulse phase estimation of x-ray crab pulsar for xnav flight experiments," *IEEE Transactions on Aerospace and Electronic Systems*, 2022.

[105] L. Hou and Z. R. Putnam, "A norm-minimization algorithm for solving the cold-start problem with xnav," *arXiv preprint arXiv:2302.06741*, 2023.

[106] A. Pantazides and D. Gebre-Egziabher, "Optimal attitude guidance for the exact and impress cubesats using graph methods with pruning," *Proceedings of the Mission Operations & Autonomy Small Satellite Conference*, 2021.

Annex: Extended abstract

The reduction in size, development time, and cost has facilitated the use of satellite constellations composed of miniaturized satellites. A particular interest in these constellations is related to probing the space environment to develop predictive models of space situational state or the so-called space weather. The desired number of satellites required to model the space dynamics usually falls in the hundreds. Also, there is a lack of measurements at altitudes below 380 km, where significant propulsion is required to maintain large satellites, making them unfeasible for that region. A potential alternative is to use femto-satellites, which have a mass of less than 100 g. These types of satellites have a low-cost development. Even if they fall to earth fast, they are so inexpensive that it is more convenient to replace them than try to keep them in orbit with propulsion. This strategy is followed by the earth observation company Planet, which uses a 100 satellite constellation of 3 kg CubeSats to image the earth as a whole every day. These satellites are launched at 400 km of altitude, then deorbiting in about a year. Therefore, Planet has to replace the entire constellation every year.

Space weather measurements (magnetospheric and ionospheric) can be performed with satellites in the range of 100 g and 1 kg. Nevertheless, the complication of using this type of satellite for space weather applications is the requirement of the precise location of the satellites. Thus, in femto-satellites is possible to use Commercial-Off-The-Shelf (COTS) components for every subsystem, except for the GNSS receiver, which is necessary for many space applications. A GNSS receiver with the license to operate in space costs around US $ 2,000. This cost can be prohibitive for a constellation of thousands of femto-satellites. Besides the cost, the power budget of a femto-satellite is not enough to handle the continuous operation of a GNSS receiver. Following that trend, in the Space and Planetary Exploration Laboratory (SPEL), I designed an experiment developing the femto-satellite FE1 carried by SUCHAI-3. For this femto-satellite, I propose to study a low-cost, low-power localization system. It consists of using two 3U CubeSats as a reference for the femto-satellite. In this localization system, only the CubeSats need a GNSS receiver to get their position, an Attitude Determination and Control System (ADCS), and an antenna array. The femto-satellite only needs a transceiver to send a beacon. The CubeSats can use these beacons to estimate the location using the Time Difference Of Arrival (TDOA) and Angle Of Arrival (AOA). I developed a platform to evaluate the impact of these strategies of space location estimation by running several simulations considering multiple deployment scenarios of the femto-satellite from the mother-CubeSat. Additionally, I will explore the performance impact of using *a priori* information of the trajectories using the Hill–Clohessy–Wiltshire dynamic model to improve the precision of the localization.